Adaptive local representations for Helmholtz Trefftz discontinuous Galerkin methods

Shelvean Kapita
Department of Mathematics, Texas A&M University, College Station, TX 77843, USA
kapita@tamu.edu

Abstract

We study the selection and stable realization of local approximation spaces in Trefftz discontinuous Galerkin discretizations of the Helmholtz equation. A scaled Cauchy-trace inner product places plane waves and Fourier–Bessel functions in a common geometry: Fourier–Bessel modes are orthogonal with explicit weights, while the same weights determine the circulant spectrum of an equispaced plane-wave trace Gram matrix. This separates amplitude scaling from genuine trace-rank loss and yields an exact best-approximation identity for mixed plane-wave–Fourier–Bessel spaces. With complex plane-wave angles, the unresolved modal tail is an exponential sequence, so propagating and evanescent components can be identified by the same ESPRIT/variable-projection procedure. We prove exact recovery and a perturbation estimate for the recovered angles and, under the standard PWDG quasi-optimality bound, transfer these perturbations to the DG error. Trace-Riesz orthonormalization is then separated from a graph–Riesz normalization of the assembled operator. Numerical experiments verify the identities, recover sparse ray fields to roundoff, and resolve a propagating-to-evanescent transition without a prescribed critical angle.

Keywords: Helmholtz equation; Trefftz discontinuous Galerkin method; plane waves; Fourier–Bessel functions; evanescent waves; ESPRIT.
2020 Mathematics Subject Classification: 65N30, 65N35, 65N50, 65F35.

1 Introduction

Trefftz methods use elementwise solutions of the governing differential equation as trial and test functions. For the homogeneous Helmholtz equation

$$\Delta u + \kappa^2 u = 0, \tag{1.1}$$

plane waves give the plane-wave discontinuous Galerkin (PWDG) and ultra-weak variational formulation (UWVF) families; see, for example, (Cessenat and Després, 1998; Gittelson et al., 2009; Hiptmair et al., 2011, 2016a). Their approximation properties are particularly attractive for locally directional wave fields. The practical difficulty is that the local representation itself may become numerically poor before the globally coupled DG problem is assembled. Crowded plane-wave directions produce strongly correlated traces, whereas high-order Fourier–Bessel (FB) functions may have very small unscaled trace amplitudes. The first effect is a loss of effective dimension; the second is largely a coordinate-scaling effect. Previous work has addressed conditioning and alternative local bases (Huttunen et al., 2002; Perrey-Debain, 2006; Luostari et al., 2012; Congreve et al., 2019;

Barucq et al., 2021), while direction-adaptive approaches optimize or infer dominant PW directions within a prescribed plane-wave family (Amara et al., 2014; Agrawal and Hoppe, 2017; Fang et al., 2017; Kapita, 2026). The present problem is different: both the directional PW component and the complementary FB component are selected in one trace metric, and unresolved local rank is removed before any global system is assembled. The local selection step is independent of whether the retained Trefftz space is subsequently coupled by PWDG or UWVF; the global conditioning analysis below is stated for the PWDG form.

Let K be contained in a disk $B(x_K, h)$ lying in one homogeneous Helmholtz region. We equip the Cauchy trace on the circle with

$$\langle v, w\rangle_{\mathrm{tr}} = \int_{\partial B(x_K,h)} \left(\kappa v\overline{w} + \kappa^{-1}\partial_n v\,\overline{\partial_n w}\right) ds. \tag{1.2}$$

For the regular Fourier–Bessel modes $\varphi_m(\rho,\psi) = J_m(\kappa\rho)e^{im\psi}$, Theorem 3.1 gives

$$\langle \varphi_m, \varphi_n\rangle_{\mathrm{tr}} = \tau_m^2\delta_{mn}, \qquad \tau_m^2 = 2\pi h\kappa\big(J_m(\kappa h)^2 + J_m'(\kappa h)^2\big), \tag{1.3}$$

and Theorem 3.4 shows that the same weights determine the eigenvalues of the trace Gram matrix of q equispaced plane waves,

$$\lambda_s = q \sum_{m\equiv -s \pmod q} \tau_m^2, \qquad s = 0,\dots,q-1. \tag{1.4}$$

Hence small FB amplitudes can be removed by trace equilibration, while small PW Gram eigenvalues identify genuine redundancy. This distinction is the basis of the local rank test used below.

The second ingredient is an exact representation formula. For a complex angle $z \in \mathbb{C}$, set

$$\psi_z(x) = e^{i\kappa d(z)\cdot(x-x_K)}, \qquad d(z) = (\cos z, \sin z). \tag{1.5}$$

Since $d(z)\cdot d(z) = 1$, ψ_z is Trefftz for every z. For a real angle θ, define the orthonormal directions

$$t_\theta = (\cos\theta, \sin\theta), \qquad t_\theta^\perp = (-\sin\theta, \cos\theta).$$

If $z = \theta + i\eta$, then $d(z) = \cosh(\eta)t_\theta + i\sinh(\eta)t_\theta^\perp$, and its oscillatory and exponential factors are

$$\psi_{\theta+i\eta} = e^{i\kappa\cosh\eta\, t_\theta\cdot(x-x_K)}e^{-\kappa\sinh\eta\, t_\theta^\perp\cdot(x-x_K)}. \tag{1.6}$$

Thus $\eta = 0$ gives propagation in direction t_θ, whereas $\eta \neq 0$ introduces exponential variation in the transverse direction $t_\theta^\perp$; propagation and evanescence belong to the same parameterization. If $u = \sum_m a_m\varphi_m$, $\gamma_m = i^{-m}a_m$, and $\mathcal{V}_{q,M}(Z_q)$ contains q complex-angle plane waves and the FB modes $|m| \le M$, Theorem 3.5 proves

$$\inf_{v\in\mathcal{V}_{q,M}(Z_q)} \|u - v\|_{\mathrm{tr}}^2 = \min_{c\in\mathbb{C}^q} \sum_{|m|>M} \tau_m^2 \left|\gamma_m - \sum_{j=1}^{q} c_j e^{-imz_j}\right|^2. \tag{1.7}$$

After the resolved FB block is removed, selecting the remaining plane waves is therefore a weighted exponential-fitting problem in the modal index.

The main analytical consequences are as follows. First, Theorems 3.1, 3.4 and 3.5 provide a common local approximation geometry for FB, PW and mixed spaces. Second, the exponential structure in (1.7) permits target-frequency direction identification by ESPRIT, followed by a small

variable-projection problem. Theorems 5.1 and 5.2 give exact recovery for finite exponential sums and perturbation stability of the recovered complex angles. Third, Theorems 5.4 and 5.5 connect these local angle perturbations to element, boundary-trace and PWDG errors; the final DG estimate is conditional only on the standard quasi-optimality bound for the fixed PWDG flux configuration. Fourth, stability is treated at two distinct levels. The selected local family is orthonormalized in the Cauchy-trace metric, whereas the assembled matrix is normalized in the DG graph metric. Theorem 2.3 shows that the latter transformation produces the normal matrix $S - iI$ with S Hermitian. Local trace rank and global operator conditioning are therefore not identified with one another.

The disk construction is a local analytical device, not a geometric restriction on the mesh. When a homogeneous continuation to a containing circle is unavailable—for example near a source, material interface, obstacle boundary or re-entrant corner—the same candidate spaces are compared by Cauchy least squares directly on the physical element boundary. The numerical experiments test both settings. They verify the trace identities independently, compare sparse and distributed angular content, exhibit the high-order rank ceiling of plane-wave traces, recover a propagating-to-evanescent transmission transition without supplying the critical angle, and compare local trace selection with a globally coupled residual search.

The paper is organized as follows. Section 2 states the Trefftz-DG formulation and graph metric. Section 3 develops the local trace identities and hybrid approximation formula. Section 4 separates effective local dimension from the conditioning of the assembled system. Section 5 develops local direction identification, variable projection and the perturbation-to-DG estimate, and then records the globally coupled residual formulation used for comparison. Section 6 presents the numerical results. Conclusions are given in Section 7.

2 Trefftz-DG formulation and graph metric

2.1 PWDG formulation and graph metric

We use $e^{-i\omega t}$, so $e^{i\kappa d\cdot x}$ propagates in direction d, outgoing cylindrical waves use $H_m^{(1)}$, and

$$\partial_n u - i\kappa u = g_A. \tag{2.1}$$

Set the dimensionless flux

$$\sigma = -\frac{1}{i\kappa}\nabla u, \qquad \nabla u + i\kappa\sigma = 0, \qquad \nabla\cdot\sigma + i\kappa u = 0. \tag{2.2}$$

Let $\mathcal{T}_h$ be a shape-regular mesh with interior faces $\mathcal{F}_h^{\mathrm{I}}$. For $F = \partial K^+ \cap \partial K^-$ with outward normals $n^\pm$,

$$\{\!\{v\}\!\} = \tfrac{1}{2}(v^+ + v^-), \quad [\![v]\!]_N = v^+n^+ + v^-n^-, \quad [\![\nabla v]\!]_N = \nabla v^+\cdot n^+ + \nabla v^-\cdot n^-, \tag{2.3}$$

where the subscript N labels a normal jump; in particular, $[\![\nabla v]\!]_N$ is a scalar normal-flux jump and not a norm of ∇v. The broken Trefftz space is $T(\mathcal{T}_h) = \{v \in H^1(\mathcal{T}_h) :\ \Delta v + \kappa^2 v = 0 \text{ in every } K \in \mathcal{T}_h\}$.

On interior faces we use the conjugated PWDG flux family (Cessenat and Després, 1998; Gittelson et al., 2009; Hiptmair et al., 2011)

$$\widehat{u} = \{\!\{u\}\!\} + \frac{\beta}{i\kappa}[\![\nabla u]\!]_N, \qquad \widehat{\sigma} = \{\!\{\sigma\}\!\} - \alpha[\![u]\!]_N, \qquad \alpha,\beta > 0. \tag{2.4}$$

On a Dirichlet boundary Γ_D with $u = g_D$ we take $\widehat{u} = g_D$ and $\widehat{\sigma} = \sigma - \alpha(u - g_D)n$. On an impedance boundary Γ_A satisfying (2.1), with $r_A(u) = \partial_n u - i\kappa u - g_A$,

$$\widehat{u} = u + \frac{\delta}{i\kappa}r_A(u), \qquad \widehat{\sigma} = \sigma - (1-\delta)\Big(\sigma\cdot n + u + \frac{g_A}{i\kappa}\Big)n, \qquad 0 < \delta < 1. \tag{2.5}$$

Unless stated otherwise, all computations use the symmetric choice $\alpha = \beta = \delta = 1/2$. The transmission tests have no impedance boundary and use $\alpha = \beta = 1/2$ with the interface scaling stated in Section 6. For Trefftz trial and test functions, elementwise Green identities leave only skeleton terms (Hiptmair et al., 2011, 2016b). The discrete problem is: find $u_h \in V_h \subset T(\mathcal{T}_h)$ with

$$\mathscr{A}_h(u_h, v_h) = \ell_h(v_h) \qquad \forall v_h \in V_h, \tag{2.6}$$

$$\begin{aligned}
\mathscr{A}_h(u,v) = & \int_{\mathcal{F}_h^{\mathrm{I}}} \Big(\{\!\{u\}\!\}\, \overline{[\![\nabla v]\!]_N} - \{\!\{\nabla u\}\!\} \cdot \overline{[\![v]\!]_N} \Big) ds \\
& - \int_{\mathcal{F}_h^{\mathrm{I}}} \Big(\alpha i\kappa [\![u]\!]_N \cdot \overline{[\![v]\!]_N} - \frac{\beta}{i\kappa} [\![\nabla u]\!]_N \, \overline{[\![\nabla v]\!]_N} \Big) ds \\
& + \int_{\Gamma_D} \Big(- \partial_n u\, \overline{v} - \alpha i\kappa u \overline{v} \Big) ds \\
& + \int_{\Gamma_A} \Big(- \delta(\partial_n u\, \overline{v} + u\, \overline{\partial_n v}) - i(1-\delta)\kappa u \overline{v} + \frac{\delta}{i\kappa} \partial_n u\, \overline{\partial_n v} \Big) ds, \qquad (2.7) \\
\ell_h(v) = & - \int_{\Gamma_D} g_D \big(\overline{\partial_n v} + \alpha i\kappa \overline{v} \big) ds \\
& + \int_{\Gamma_A} \Big((1-\delta) g_A \overline{v} + \frac{\delta}{i\kappa} g_A \overline{\partial_n v} \Big) ds. \qquad (2.8)
\end{aligned}$$

With this convention the penalty terms have negative imaginary part because $1/i = -i$. For $v \in T(\mathcal{T}_h)$ one obtains the graph identity, the analogue of the coercive skeleton norm of PWDG analysis (Gittelson et al., 2009; Hiptmair et al., 2011),

$$\begin{aligned}
-\operatorname{Im} \mathscr{A}_h(v,v) = {} & \alpha\kappa \|[\![v]\!]_N\|^2_{0,\mathcal{F}_h^{\mathrm{I}}} + \beta\kappa^{-1} \|[\![\nabla v]\!]_N\|^2_{0,\mathcal{F}_h^{\mathrm{I}}} + \alpha\kappa \|v\|^2_{0,\Gamma_D} \\
& + (1-\delta)\kappa \|v\|^2_{0,\Gamma_A} + \delta\kappa^{-1} \|\partial_n v\|^2_{0,\Gamma_A}.
\end{aligned} \tag{2.9}$$

Thus, if K_h is the stiffness matrix of (2.6), the positive graph matrix is

$$G_h := \frac{K_h^* - K_h}{2i} > 0. \tag{2.10}$$

The sign is convention dependent; under $e^{+i\omega t}$ the opposite sign is positive.

Proposition 2.1 (Definiteness of the PWDG graph metric)**.** *Assume $\alpha, \beta > 0$ and $0 < \delta < 1$. If Γ_A contains a nonempty relatively open boundary segment, then the right-hand side of (2.9) is a norm on every finite-dimensional Trefftz space V_h. If $\Gamma_A = \varnothing$, the same conclusion holds provided κ^2 is not a Dirichlet eigenvalue of $-\Delta$ on Ω. Consequently, in either case $G_h > 0$ for every linearly independent coefficient basis of V_h.*

Proof. If the graph seminorm of $v \in V_h$ vanishes, both the value and normal-flux jumps vanish on every interior face. Hence the broken Trefftz field is a global Helmholtz solution with continuous Cauchy data across the mesh. On Γ_D its trace is zero. If $\Gamma_A \neq \varnothing$, (2.9) also gives $v = \partial_n v = 0$ on an open boundary segment, so Cauchy uniqueness gives $v = 0$. If $\Gamma_A = \varnothing$, the homogeneous Dirichlet problem has only the zero solution by the nonresonance hypothesis. Positivity of the Gram matrix follows. □

Remark 2.2 (Interior resonance)**.** *When $\Gamma_A = \varnothing$, the exclusion of Dirichlet eigenfrequencies is a property of the underlying boundary-value problem, not of the local representation. Away from exact resonance G_h is positive, but the continuous resolvent and the corresponding quasi-optimality constants can deteriorate as κ^2 approaches the Dirichlet spectrum. Representation selection and graph–Riesz normalization do not remove this loss of problem stability. For exterior-scattering computations the impedance or DtN boundary terms used here avoid this pure-Dirichlet situation; for an interior problem resonance must be treated at the PDE level, for example by changing the boundary condition or by using a shifted formulation appropriate to the application.*

For the truncated nonlocal DtN form we use the corresponding coercivity result of Kapita and Monk (2018); in floating point the Cholesky test remains an implementation check on the retained coordinates, not the source of continuous stability.

2.2 DtN truncation and graph–Riesz coordinates

The scattering experiments use a circular Dirichlet-to-Neumann (DtN) boundary $r = R$. A first-order absorbing condition would add reflection error to the same traces used to judge the local representation, while the Fourier–Hankel DtN map removes that ambiguity, so changes in the error can be attributed to the local representation alone. Circular DtN maps are classical exact nonreflecting boundary conditions (Keller and Givoli, 1989), follow from separation of variables (Colton and Kress, 2013), and were used with PWDG by Kapita and Monk (2018). The truncated map and residual are

$$\mathrm{DtN}_N\, v = \sum_{|m|\le N} \kappa \frac{H_m^{(1)\prime}(\kappa R)}{H_m^{(1)}(\kappa R)} v_m e^{im\theta}, \qquad r_N(u) = \partial_n u - \mathrm{DtN}_N\, u - g_R, \tag{2.11}$$

with the nonlocal flux pair

$$\widehat{u} = u + \frac{\delta}{i\kappa} r_N(u), \qquad i\kappa\, \widehat{\sigma}\cdot n = -(\mathrm{DtN}_N\, u + g_R) - \frac{\delta}{i\kappa}\, \mathrm{DtN}_N^*\, r_N(u). \tag{2.12}$$

For homogeneous data the boundary form is

$$\mathscr{A}_R(u,v) = \int_{\Gamma_R} \Big[u\,\overline{\partial_n v} - (\mathrm{DtN}_N\, u)\overline{v} + \frac{\delta}{i\kappa}(\partial_n u - \mathrm{DtN}_N\, u)\overline{(\partial_n v - \mathrm{DtN}_N\, v)} \Big] ds, \tag{2.13}$$

the $H^{(1)}$ conjugate of the form in Kapita and Monk (2018). In the computations we form G_h from (2.10) and verify definiteness numerically.

After the local space has been fixed, the assembled operator is normalized in the graph metric. Let $K_h \in \mathbb{C}^{n_h\times n_h}$ be the PWDG matrix after local selection and trace orthonormalization, and write

$$H_h := \frac{K_h + K_h^*}{2}, \qquad G_h := \frac{K_h^* - K_h}{2i}, \qquad K_h = H_h - iG_h. \tag{2.14}$$

For the stable fluxes used here $G_h = G_h^* > 0$ on the retained space. Let B satisfy

$$B^* G_h B = I. \tag{2.15}$$

The implementation uses $G_h = LL^*$ and $B = L^{-*}$; failure of the Cholesky factorization makes the retained space inadmissible. Any two exact factors satisfying (2.15) differ by a unitary matrix.

Proposition 2.3 (Graph–Riesz normal form)**.** *Let*

$$\widehat{K}_h := B^* K_h B, \qquad S := B^* H_h B. \tag{2.16}$$

Then $\widehat{K}_h = S - iI$ *with* $S = S^*$*. Hence* $\widehat{K}_h$ *is normal,*

$$\sigma_j(\widehat{K}_h) = \sqrt{1 + \lambda_j(S)^2}, \qquad \sigma_{\min}(\widehat{K}_h) \geq 1. \tag{2.17}$$

Proof. $S = B^* H_h B$ is Hermitian and (2.15) gives $B^* K_h B = B^* H_h B - iB^* G_h B = S - iI$. A Hermitian matrix commutes with the identity, so $S - iI$ is normal. Its singular values are the moduli of the eigenvalues $\lambda_j(S) - i$, which gives (2.17). □

In exact arithmetic, (2.15) gives

$$\kappa_{\mathrm{GR}} := \kappa_2(\widehat{K}_h) = \frac{\max_j \sqrt{1 + \lambda_j(S)^2}}{\min_j \sqrt{1 + \lambda_j(S)^2}}. \tag{2.18}$$

Thus $\sigma_{\min}(\widehat{K}_h) \geq 1$ and growth of κ_{GR} is governed by the Hermitian part S. Numerical values of κ_{GR} are computed by SVD of the actual floating-point matrix $B^* K_h B$. Local rank decisions use only the trace metric; κ_{GR} measures the final globally coupled solve.

3 Local Cauchy-trace geometry

3.1 Trace metric and modal identities

Fix K and a disk $B_K = B(x_K, h) \supset K$ contained in the same homogeneous Helmholtz region. This local analyticity assumption is the only role of the disk; near sources, interfaces, or obstacle boundaries the selector instead uses element-boundary trace fitting. Regular Helmholtz fields on B_K admit the Fourier–Bessel expansion (Watson, 1944; Moiola et al., 2011). Write

$$r_K := \sup_{x \in K} |x - x_K|, \qquad d_K := \operatorname{dist}(x_K, \Sigma_K), \tag{3.1}$$

where Σ_K is the nearest source, material interface, obstacle boundary, or other set across which the same regular Helmholtz continuation is unavailable. The disk construction is admissible whenever

$$r_K < h < d_K. \tag{3.2}$$

All identities below hold for every such h. Numerically, h also fixes κh and hence the modal weights τ_m; it is therefore part of the rank-resolution scale, not a physical mesh parameter. We use the smallest convenient containing disk with a modest geometric margin. If (3.2) is empty, no disk continuation is invoked and the same candidate spaces are compared by Cauchy least squares on ∂K.

$$u(\rho, \psi) = \sum_{m \in \mathbb{Z}} a_m \varphi_m(\rho, \psi), \qquad \varphi_m = J_m(\kappa\rho) e^{im\psi}, \tag{3.3}$$

and on ∂B_K we define the scaled Cauchy trace inner product

$$\langle v, w \rangle_{\mathrm{tr}} = \int_{\partial B_K} \left(\kappa v \overline{w} + \kappa^{-1} \partial_n v \, \overline{\partial_n w} \right) ds. \tag{3.4}$$

The weights are the value/flux scaling of the PWDG graph norm.

The Fourier–Bessel basis diagonalizes this metric.

Theorem 3.1 (Trace orthogonality)**.** *The functions φ_m are orthogonal in* (3.4)*:*

$$\langle \varphi_m, \varphi_n \rangle_{\mathrm{tr}} = \tau_m^2 \delta_{mn}, \qquad \tau_m^2 = 2\pi h\kappa \big(J_m(\kappa h)^2 + J_m'(\kappa h)^2 \big), \tag{3.5}$$

and $\tau_m > 0$ for every m when $\kappa h > 0$.

Proof. On $\rho = h$, $\varphi_m = J_m(\kappa h) e^{im\psi}$ and $\partial_n \varphi_m = \kappa J_m'(\kappa h) e^{im\psi}$. Substitute into (3.4) with $ds = h\, d\psi$ and use Fourier orthogonality. If J_m and J_m' vanished at the same $z > 0$, uniqueness for the Bessel equation with zero Cauchy data would give $J_m \equiv 0$. □

Corollary 3.2 (Equilibrated modal isometry)**.** *If u has the expansion* (3.3)*, then*

$$\|u\|_{\mathrm{tr}}^2 = \sum_{m \in \mathbb{Z}} |a_m|^2 \tau_m^2, \tag{3.6}$$

and the quantities

$$b_m := \tau_m a_m = \big\langle u, \varphi_m / \tau_m \big\rangle_{\mathrm{tr}} \tag{3.7}$$

are orthonormal coordinates of the trace. The map $u \mapsto (b_m)$ is an isometry into ℓ^2.

Remark 3.3. *The isometry concerns the equilibrated coefficients b_m, not the raw coefficients $a_m = b_m/\tau_m$. At high order τ_m is very small (Fig. 1a), so recovering unscaled a_m amplifies roundoff. Rank decisions must be made after trace equilibration.*

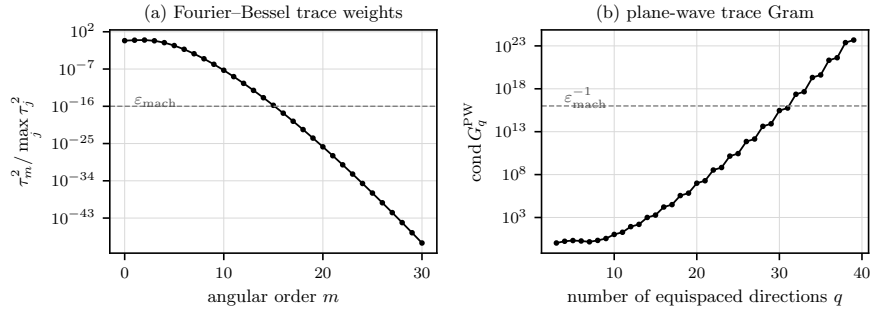


Figure 1: Local trace geometry at $k = 16$ and $kh = 3.34$. Left: Fourier–Bessel trace weights τ_m. Right: condition number of the equispaced plane-wave trace Gram matrix obtained from (3.10).

The same weights also determine the spectrum of equispaced propagating plane-wave traces. For $z \in \mathbb{C}$ let ψ_z be (1.5). Jacobi–Anger gives, first for real z and then for complex z by analytic continuation,

$$\psi_z(\rho, \psi) = \sum_{m \in \mathbb{Z}} i^m J_m(\kappa\rho) e^{im\psi} e^{-imz}. \tag{3.8}$$

Thus the phase-corrected modal sequence of one complex-angle plane wave is e^{-imz}.

Theorem 3.4 (Plane-wave Gram symbol)**.** *For real angles θ_j, θ_ℓ,*

$$\langle \psi_{\theta_j}, \psi_{\theta_\ell} \rangle_{\mathrm{tr}} = \sum_{m \in \mathbb{Z}} \tau_m^2 e^{-im(\theta_j - \theta_\ell)}. \tag{3.9}$$

If $\theta_j = 2\pi j/q$, $j = 0, \dots, q-1$, then G_q^{PW} is circulant with

$$\lambda_s = q \sum_{m \equiv -s \pmod q} \tau_m^2, \qquad s = 0, \dots, q-1. \tag{3.10}$$

Proof. Insert (3.8) into (3.4) and use Theorem 3.1. For equispaced real angles, a discrete Fourier transform leaves precisely the residue classes in (3.10). □

Small PW eigenvalues are therefore correlation, not amplitude scaling; diagonal equilibration cannot remove them.

3.2 Hybrid approximation and representation crossover

For $Z_q = (z_1, \dots, z_q) \in \mathbb{C}^q$ define

$$\mathcal{V}_{q,M}(Z_q) = \operatorname{span}\{\psi_{z_j} : 1 \le j \le q\} + \operatorname{span}\{\varphi_m : |m| \le M\}. \tag{3.11}$$

Theorem 3.5 (Hybrid error)**.** *Let u satisfy* (3.3)*, $\gamma_m = i^{-m} a_m$, and $|\operatorname{Im} z_j| \le \eta_{\max} < \infty$. Then*

$$\inf_{v \in \mathcal{V}_{q,M}(Z_q)} \|u - v\|_{\mathrm{tr}}^2 = \min_{c \in \mathbb{C}^q} \sum_{|m|>M} \tau_m^2 \left| \gamma_m - \sum_{j=1}^{q} c_j e^{-imz_j} \right|^2. \tag{3.12}$$

Repeated angles are allowed; they only make the PW coefficient vector nonunique.

Proof. By (3.8), the PW block contributes $\sum_j c_j e^{-imz_j}$ after removal of the phase i^m. The bounded-strip hypothesis and the factorial decay of $J_m(\kappa h)$ and $J_m'(\kappa h)$ imply $\tau_m e^{|m|\eta_{\max}} \in \ell^2$, so the weighted modal series is well defined. For fixed c, the FB coefficients with $|m| \le M$ cancel the low-order residual exactly. Apply Theorem 3.2 to the remaining tail and minimize over c. □

Corollary 3.6 (Sparse complex rays)**.** *If u is a superposition of q_* plane waves ψ_{z_j} whose distinct complex angles are contained in Z_q, then the right side of* (3.12) *vanishes for $q \ge q_*$, independently of M.*

Proof. Choose the generating PW coefficients and set the others to zero. Equation (3.8) reproduces every modal coefficient. □

The hybrid identity also yields an exact field-dependent crossover criterion. Let

$$u(\rho) = u_{\mathrm{ray}} + \rho u_{\mathrm{diff}}, \qquad \rho \ge 0, \tag{3.13}$$

where u_{ray} is a finite ray field and u_{diff} has nonsparse equilibrated modal content on the resolved window. Let $g_{\mathrm{ray}}, g_{\mathrm{diff}} \in \ell^2$ be their equilibrated coefficient vectors from Theorem 3.2; hence

$$g(\rho) = g_{\mathrm{ray}} + \rho g_{\mathrm{diff}}. \tag{3.14}$$

For a fixed candidate space V, let P_V be the orthogonal projector onto its equilibrated modal image. Then

$$E_V(\rho)^2 := \inf_{v \in V} \|u(\rho) - v\|_{\mathrm{tr}}^2 = \|(I - P_V) g(\rho)\|_2^2 = A_V + 2\rho B_V + \rho^2 C_V, \tag{3.15}$$

where, with $r_{\mathrm{ray}} = (I - P_V) g_{\mathrm{ray}}$ and $r_{\mathrm{diff}} = (I - P_V) g_{\mathrm{diff}}$,

$$A_V = \|r_{\mathrm{ray}}\|_2^2, \qquad B_V = \operatorname{Re}(r_{\mathrm{ray}}^* r_{\mathrm{diff}}), \qquad C_V = \|r_{\mathrm{diff}}\|_2^2. \tag{3.16}$$

For two candidate spaces V_1 and V_2, equality of the two errors is equivalent to

$$(C_{V_1} - C_{V_2})\rho^2 + 2(B_{V_1} - B_{V_2})\rho + (A_{V_1} - A_{V_2}) = 0. \tag{3.17}$$

Thus the representation crossover is obtained from a scalar quadratic. If (3.17) has no nonnegative real root, the ordering of V_1 and V_2 is fixed for all $\rho \ge 0$; otherwise its nonnegative roots partition that half-line into intervals of fixed ordering. No DG solve is required for this comparison.

4 Stable local coordinates and effective trace dimension

For a selected local family $\Psi_K = [\psi_1, \dots, \psi_{p_K}]$, define

$$G^{\mathrm{tr}}_{K,\mathrm{raw}} = \big(\langle \psi_j, \psi_\ell \rangle_{\mathrm{tr},K}\big)_{j,\ell}, \qquad D_K = \mathrm{diag}\,\big(\|\psi_j\|^{-1}_{\mathrm{tr},K}\big), \qquad G^{\mathrm{tr}}_{K,\mathrm{eq}} = D^*_K G^{\mathrm{tr}}_{K,\mathrm{raw}} D_K. \tag{4.1}$$

The diagonal scaling removes trace amplitude; the spectrum of $G^{\mathrm{tr}}_{K,\mathrm{eq}}$ measures correlation. For a Hermitian positive semidefinite Gram matrix G, set

$$r_{\mathrm{eff}}(G;\varepsilon) = \#\{j : \lambda_j(G) \geq \varepsilon \lambda_{\max}(G)\}. \tag{4.2}$$

PW directions are retained only when the equilibrated PW block has full nominal rank. FB modes are equilibrated before any rank decision; the complete hybrid block is then tested for cross-family redundancy. If T_K is the resulting trace-Riesz map,

$$T^*_K G^{\mathrm{tr}}_{K,\mathrm{raw}} T_K = I, \qquad \kappa_{\mathrm{tr,final}} := \max_K \kappa_2(T^*_K G^{\mathrm{tr}}_{K,\mathrm{raw}} T_K). \tag{4.3}$$

This is a local coordinate quantity. The assembled PWDG operator has the separate graph–Riesz condition number κ_{GR} of (2.18).

Table 1: Local trace-Gram condition numbers at $\kappa h = 3.34$. PW columns are unscaled; the FB column is trace-equilibrated.

local count	PW Gram, disk	PW Gram, element	equilibrated FB, element
9	3.6	1.7×10^1	1.95
15	1.9×10^3	4.8×10^4	9.9
21	2.0×10^7	2.6×10^9	7.0×10^1
27	1.4×10^{12}	8.5×10^{14}	5.0×10^2
33	$> 10^{15}$	rank deficient	4.2×10^3

The selected local space is orthonormalized in the trace metric before global assembly. Local rank loss is removed before global coupling (Huttunen et al., 2002; Congreve et al., 2019; Barucq et al., 2021).

Scale the selected family by D_K. Apply the rank threshold to the equilibrated PW block, retain resolvable FB modes, then apply the same threshold to the full hybrid Gram to remove cross-family redundancy. If Q_r, Λ_r are the retained eigendata of the resulting raw trace Gram, define

$$\Phi_K = \Psi_K T_K, \qquad T_K = Q_r \Lambda_r^{-1/2}, \qquad T^*_K G^{\mathrm{tr}}_{K,\mathrm{raw}} T_K = I. \tag{4.4}$$

All subsequent assembly uses the retained trace-orthonormal space. In floating point we report the condition number of the recomputed matrix $T^*_K G^{\mathrm{tr}}_{K,\mathrm{raw}} T_K$. Thus T_K is obtained explicitly from the retained eigenpairs of the local Gram matrix, not from an additional optimization problem. If p_K local functions are sampled at Q_K trace quadrature points, forming the Gram matrix costs $O(Q_K p_K^2)$ and its Hermitian eigendecomposition costs $O(p_K^3)$; both operations are element local and are performed once before global assembly.

The transformations act on different objects: T_K fixes the local representation; B normalizes the assembled PWDG operator.

Table 2 separates the local and global condition numbers. The PW rows lose redundant directions before assembly; the FB rows retain their equilibrated dimensions.

For any recovered PW candidate Z_q, admissibility means

$$r_{\mathrm{eff}}(G^{\mathrm{PW}}_q(Z_q); \varepsilon_{\mathrm{solve}}) = q. \tag{4.5}$$

Algorithm 1 Local conditioning and global graph–Riesz solve

for each element K **do**
  select the family Ψ_K (PW, FB, or mixed) by Algorithm 2;
  scale every basis function by its local trace norm;
  diagonalize the equilibrated PW trace Gram matrix and discard eigenvectors with $\lambda < \tau_{\mathrm{rank}}\lambda_{\max}$;
  retain the equilibrated FB block unless it is numerically null;
  diagonalize the retained full hybrid trace Gram matrix, remove any cross-family eigenvectors below the same rank tolerance, and store the trace-Riesz map T_K.
end for
assemble the Trefftz-DG system in the block-diagonal conditioned coordinates;
form $G_h = (K_h^* - K_h)/(2i)$, verify $\lambda_{\min}(G_h) > 0$, compute a Cholesky factor $G_h = LL^*$, and set $B = L^{-*}$;
solve $(B^*K_hB)\widehat{c} = B^*f$ and back-transform.

Table 2: Local and global conditioning at $\kappa = 8$ on eight curved sectors. $\kappa_{\mathrm{tr,raw}}$ is the worst raw local trace-Gram condition number; $\kappa_{\mathrm{tr,final}}$ is measured after trace orthonormalization; κ_{GR} belongs to the assembled graph–Riesz PWDG matrix.

p	$(q_{\mathrm{PW}}, q_{\mathrm{FB}})$	retained	$\kappa_{\mathrm{tr,raw}}$	$\kappa_{\mathrm{tr,final}}$	κ_{GR}
15	$(15, 0)$	104	9.6×10^{13}	1.000001	3.12
15	$(0, 15)$	120	4.9×10^{4}	1.000000	3.67
15	$(7, 8)$	120	2.8×10^{10}	1.000002	3.63
27	$(27, 0)$	120	1.2×10^{18}	1.000001	4.00
27	$(0, 27)$	216	8.9×10^{14}	1.000000	7.93
27	$(11, 16)$	168	1.4×10^{19}	1.000006	5.37

For equispaced real angles the eigenvalues are given explicitly by Theorem 3.4. The parameter $\varepsilon_{\mathrm{solve}}$ denotes the smallest relative trace scale that the subsequent numerical solve is intended to resolve, and τ_{rank} is the relative eigenvalue threshold used in the local Gram matrices. They are numerical-accuracy parameters, not physical parameters and not universal constants. For clarity, let $\varepsilon_{\mathrm{floor}} := \max\{\varepsilon_{\mathrm{mach}}, \varepsilon_{\mathrm{lin}}, \varepsilon_{\mathrm{data}}\}$ denote an estimated relative numerical floor, where $\varepsilon_{\mathrm{lin}}$ is the attained relative linear-algebra accuracy and $\varepsilon_{\mathrm{data}}$ is the relative uncertainty of the trace data. A practical choice should satisfy $\varepsilon_{\mathrm{solve}} \gtrsim \varepsilon_{\mathrm{floor}}$. The reported binary64 direct-solve experiments use $\tau_{\mathrm{rank}} = \varepsilon_{\mathrm{solve}} = 10^{-12}$ unless a sensitivity sweep states otherwise. The wavenumber and trace radius enter indirectly through the Gram spectrum and the resolvable modal window rather than through a separate prescribed scaling of $\varepsilon_{\mathrm{solve}}$.

5 Direction identification and local optimization

The hybrid identity (1.7) turns local PW selection into a small exponential-fitting problem. We first develop this local procedure and its stability, and only afterwards record the globally coupled residual formulation used as a cost comparison in Section 6.

5.1 Local modal variable projection

The local nonlinear problem is the hybrid identity itself. For unresolved modes $|m| > M$, define

$$W(Z)_{m,j} = e^{-imz_j}, \qquad A(Z) = D_\tau W(Z), \qquad y = D_\tau \gamma, \tag{5.1}$$

where $D_\tau = \mathrm{diag}(\tau_m)$. Then

$$F_{q,M}(Z, \bar{Z}) = \min_{c \in \mathbb{C}^q} \|y - A(Z)c\|_2^2. \tag{5.2}$$

On a constant-rank stratum let $c = A^\dagger y$ and $r = y - Ac$. The envelope theorem and $A_{\bar{z}_j} = 0$ give the Wirtinger derivative

$$\partial_{\bar{z}_j} F_{q,M} = -\overline{c_j}\,(\partial_{z_j} a_j)^* r, \qquad (\partial_{z_j} a_j)_m = -im\tau_m e^{-imz_j}, \tag{5.3}$$

where a_j is the jth column of A. Coefficients are computed by QR or SVD, not by forming normal equations. Thus each trial uses only small element-local dense linear algebra; the admissible strip $|\operatorname{Im} z_j| \le \eta_{\max}$ prevents arbitrarily growing evanescent PWs.

5.2 Stability-aware local selection

For each element the selector returns an admissible (q, M, Z_q). It acts on equilibrated modal data and enforces trace rank before comparing approximation errors.

Modal recovery By Theorem 3.2 the stable quantities are $b_m = \langle u, \varphi_m/\tau_m \rangle_{\mathrm{tr}}$. We use a consecutive modal window

$$\mathcal{W} = \{m_0, m_0 + 1, \ldots, m_0 + N - 1\}$$

on which the conversion from equilibrated coefficients to γ_m is resolved: τ_m is large enough that the estimated perturbation of b_m/τ_m remains below the requested modal accuracy. The phase-corrected sequence $\gamma_m = i^{-m} b_m/\tau_m$ is analyzed for exponential structure. Reindexing by $\widetilde{\gamma}_r = \gamma_{m_0+r}$ changes only the exponential coefficients, not the nodes $\zeta_j = e^{-iz_j}$, because $\zeta_j^{m_0}$ is absorbed into the corresponding coefficient.

On a containing circle the quantities b_m are Fourier coefficients of the scaled Cauchy data. With Q trace samples, direct projection onto N retained modes costs $O(QN)$ per element; with equispaced samples the Fourier part can be evaluated simultaneously by an FFT in $O(Q \log Q)$. This trace extraction is performed once per selection update, not at every variable-projection trial. When the containing-circle hypothesis fails, no modal inversion is attempted: the candidate spaces are compared directly by Cauchy least squares on the physical element boundary.

ESPRIT for sparse exponential content For a finite complex-ray field $u_{\mathrm{ray}} = \sum_{j=1}^{q_*} c_j \psi_{z_j}$, (3.8) gives

$$\gamma_m = \sum_{j=1}^{q_*} c_j \zeta_j^m, \qquad \zeta_j = e^{-iz_j} \neq 0. \tag{5.4}$$

Thus propagation ($\operatorname{Im} z_j = 0$) corresponds to $|\zeta_j| = 1$, whereas an evanescent PW has $|\zeta_j| \neq 1$. For the reindexed window $\widetilde{\gamma}_0, \ldots, \widetilde{\gamma}_{N-1}$ we use, unless stated otherwise, the balanced dimensions

$$L = \left\lceil \frac{N+1}{2} \right\rceil, \qquad K = N - L + 1,$$

so that $L+K-1=N$. A requested rank q is admissible only when $L \geq q+1$ and $K \geq q$. We form

$$H = (\widetilde{\gamma}_{r+s})_{r=0,\dots,L-1}^{s=0,\dots,K-1}. \tag{5.5}$$

The dominant q-dimensional left singular subspace is retained only when its qth singular value is above the corresponding data-accuracy floor. If $U \in \mathbb{C}^{L\times q}$ spans that subspace and U_0, U_1 delete its last and first rows, respectively, set

$$S = U_0^{\dagger} U_1. \tag{5.6}$$

Theorem 5.1 (Exact target-frequency recovery)**.** *Assume* (5.4) *has exactly q nonzero coefficients and pairwise distinct nodes ζ_j. If $L \geq q+1$ and $K \geq q$, then* $\operatorname{rank} H = q$*, U_0 has full column rank, and*

$$S = T^{-1} \operatorname{diag}(\zeta_1, \dots, \zeta_q) T \tag{5.7}$$

for a nonsingular T. Hence ESPRIT recovers every ζ_j exactly and the complex angles follow from

$$z_j = i \operatorname{Log} \zeta_j \pmod{2\pi}, \tag{5.8}$$

with a fixed logarithm branch.

Proof. Let $(V_L)_{rj} = \zeta_j^r$, $(V_K)_{sj} = \zeta_j^s$, and $C = \operatorname{diag}(c_j)$. Then

$$H = V_L C V_K^T. \tag{5.9}$$

Distinct nodes and nonzero coefficients give $\operatorname{rank} H = q$ and $U = V_L T$ for some nonsingular T. If V_0, V_1 are the shifted row blocks of V_L, then

$$V_1 = V_0 \operatorname{diag}(\zeta_1, \dots, \zeta_q). \tag{5.10}$$

Since V_0 has full column rank, multiplication by $U_0^{\dagger}$ yields (5.7). □

Theorem 5.2 (Perturbation of ESPRIT nodes and complex angles)**.** *Let $\widetilde{H} = H + E$ and construct $\widetilde{S}$ from the dominant q-dimensional left singular subspace of $\widetilde{H}$. Put*

$$\sigma_* := \sigma_q(H) > 0, \qquad s_* := \sigma_q(U_0) > 0.$$

For sufficiently small $\|E\|_2$, the eigenvalues $\widetilde{\zeta}_j$ of $\widetilde{S}$ can be labeled so that

$$\max_j |\widetilde{\zeta}_j - \zeta_j| \leq C_{\mathrm{E}} \|E\|_2, \tag{5.11}$$

where C_{E} depends on σ_*^{-1}, s_*^{-1}, and $\kappa_2(T)$. If the exact nodes lie in a compact annulus that avoids the chosen logarithm cut, then

$$\max_j |\widetilde{z}_j - z_j| \leq C_{\log} C_{\mathrm{E}} \|E\|_2, \qquad \widetilde{z}_j = i \operatorname{Log} \widetilde{\zeta}_j. \tag{5.12}$$

Proof. Wedin's singular-subspace bound gives $\|\widetilde{U}Q - U\|_2 \leq C\|E\|_2/\sigma_*$ for a unitary Q. Since $s_* > 0$, the shifted pseudoinverse is locally Lipschitz, hence $\|Q^*\widetilde{S}Q - S\|_2 \leq C'\|E\|_2$. Bauer–Fike applied to (5.7) gives (5.11). The logarithm is locally Lipschitz on any compact set separated from zero and its branch cut, which gives (5.12). □

Corollary 5.3 (Consistency inside the hybrid selector)**.** *If*

$$\gamma_m^{(M)} = \sum_{j=1}^{q} c_j \zeta_j^m + r_m^{(M)} \tag{5.13}$$

with distinct nonzero ζ_j, and the Hankel matrix generated by $r_m^{(M)}$ tends to zero in spectral norm, then the recovered nodes and complex angles converge, up to permutation, to the exact ones. The same conclusion holds with an additional vanishing trace-discretization perturbation.

Proof. Apply Theorem 5.2 to the total Hankel perturbation. □

Lemma 5.4 (Complex-angle Lipschitz bounds)**.** *Let $K \subset B(x_K, h_K)$ and $|\operatorname{Im} z|, |\operatorname{Im} w| \le \eta_{\max}$. Define*

$$D_\eta = \sqrt{\cosh(2\eta_{\max})}, \qquad E_K = e^{\kappa h_K \sinh \eta_{\max}},$$

and introduce the augmented element-boundary norm

$$\|v\|_{\partial K,+}^2 := \int_{\partial K} \left(\kappa |v|^2 + \kappa^{-1} |\nabla v|^2\right) ds. \tag{5.14}$$

Then

$$\|\psi_z^K - \psi_w^K\|_{H^1(K)} \le C_{H^1,K} |z - w|, \tag{5.15}$$

$$\|\psi_z^K - \psi_w^K\|_{\mathrm{tr},K} \le C_{\mathrm{tr},K} |z - w|, \tag{5.16}$$

$$\|\psi_z^K - \psi_w^K\|_{\partial K,+} \le C_{\partial,K} |z - w|, \tag{5.17}$$

where one may take

$$C_{H^1,K} = |K|^{1/2} \kappa D_\eta E_K \Big(h_K^2 + (1 + \kappa h_K D_\eta)^2\Big)^{1/2}, \tag{5.18}$$

$$C_{\mathrm{tr},K} = \Big(2\pi h_K \kappa D_\eta^2 E_K^2 [(\kappa h_K)^2 + (1 + \kappa h_K D_\eta)^2]\Big)^{1/2}, \tag{5.19}$$

$$C_{\partial,K} = \Big(|\partial K|\, \kappa D_\eta^2 E_K^2 [(\kappa h_K)^2 + (1 + \kappa h_K D_\eta)^2]\Big)^{1/2}. \tag{5.20}$$

For $\eta_{\max} = 0$ these reduce to the corresponding real-angle bounds. The factor $E_K = e^{\kappa h_K \sinh \eta_{\max}}$ is intrinsic: strongly evanescent directions are exponentially amplified when continued across a patch of radius comparable with h_K. This is the reason for imposing a bounded complex-angle strip rather than allowing arbitrarily large $|\operatorname{Im} z|$.

Proof. Along the segment joining z and w,

$$\partial_z \psi_z = i\kappa d'(z) \cdot (x - x_K) \psi_z, \qquad \partial_z \nabla \psi_z = i\kappa d'(z) \psi_z + i\kappa d(z) \partial_z \psi_z.$$

On the strip, $\|d(z)\|_2, \|d'(z)\|_2 \le D_\eta$ and $|\psi_z| \le E_K$. Hence, uniformly for $x \in B(x_K, h_K)$,

$$|\partial_z \psi_z| \le \kappa D_\eta h_K E_K, \qquad |\partial_z \nabla \psi_z| \le \kappa D_\eta E_K (1 + \kappa h_K D_\eta).$$

Integration along the segment in the complex-angle plane gives the pointwise difference bounds. Integration over K, over $\partial B(x_K, h_K)$, and over ∂K, respectively, yields (5.15)–(5.17). On the circle, $|\partial_n v| \le |\nabla v|$, which gives (5.19). □

For the bridge estimate we use the standard PWDG continuity norm

$$\|v\|_{\mathrm{DG}+}^2 := -\operatorname{Im}\mathscr{A}_h(v,v) + \kappa^{-1}\|\{\!\{\nabla v\}\!\}\|_{0,\mathcal{F}_h^{\mathrm{I}}}^2 + \kappa\|\{\!\{v\}\!\}\|_{0,\mathcal{F}_h^{\mathrm{I}}}^2 + \kappa^{-1}\|\partial_n v\|_{0,\Gamma_D}^2, \tag{5.21}$$

with the finite-dimensional DtN trace terms added on Γ_R when (2.13) is used. The face inequalities for jumps and averages imply that, for piecewise Trefftz v,

$$\|v\|_{\mathrm{DG}+}^2 \le C_{\mathrm{face}} \sum_{K\in\mathcal{T}_h} \|v\|_{\partial K,+}^2, \tag{5.22}$$

where C_{face} depends only on the fixed flux parameters and face multiplicity; for a fixed truncated DtN map it also contains its finite-dimensional trace-operator bound. This is the only mesh-level constant needed below.

Theorem 5.5 (From modal perturbation to PWDG error)**.** *Suppose*

$$u|_K = \sum_{j=1}^{q_K} c_{Kj}\psi_{z_{Kj}}^K, \qquad |\operatorname{Im} z_{Kj}| \le \eta_{\max}, \tag{5.23}$$

and let the recovered angles $\widehat{z}_{Kj}$ lie in the same strip. Set

$$\delta_K^2 = \sum_{j=1}^{q_K} |\widehat{z}_{Kj} - z_{Kj}|^2.$$

If $V_h(\widehat{Z})$ contains the corresponding recovered plane waves, then

$$\inf_{v_h\in V_h(\widehat{Z})} \Big(\sum_K \|u-v_h\|_{H^1(K)}^2\Big)^{1/2} \le \Big(\sum_K C_{H^1,K}^2\|c_K\|_2^2\delta_K^2\Big)^{1/2}, \tag{5.24}$$

$$\inf_{v_h\in V_h(\widehat{Z})} \Big(\sum_K \|u-v_h\|_{\mathrm{tr},K}^2\Big)^{1/2} \le \Big(\sum_K C_{\mathrm{tr},K}^2\|c_K\|_2^2\delta_K^2\Big)^{1/2}. \tag{5.25}$$

If the standard PWDG quasi-optimality estimate

$$\|u-u_h\|_{\mathrm{DG}} \le C_{\mathrm{qo}} \inf_{v_h\in V_h(\widehat{Z})} \|u-v_h\|_{\mathrm{DG}+} \tag{5.26}$$

holds for the fixed flux configuration, then

$$\|u-u_h(\widehat{Z})\|_{\mathrm{DG}} \le C_{\mathrm{qo}}C_{\mathrm{face}}^{1/2}\Big(\sum_K C_{\partial,K}^2\|c_K\|_2^2\delta_K^2\Big)^{1/2}. \tag{5.27}$$

Proof. Use the comparison function $v_K = \sum_j c_{Kj}\psi_{\widehat{z}_{Kj}}^K$. Applying Theorem 5.4 to each summand and then Cauchy–Schwarz in the ray index gives (5.24) and (5.25); the same argument with (5.17) yields

$$\sum_K \|u-v_h\|_{\partial K,+}^2 \le \sum_K C_{\partial,K}^2\|c_K\|_2^2\delta_K^2.$$

Combine this inequality with (5.22) and (5.26) to obtain (5.27). □

The estimate inherits the stability constant C_{qo} of the underlying PWDG formulation. No uniformity of this constant is asserted near interior resonances, on strongly under-resolved meshes, or in coefficient-contrast regimes outside the hypotheses of the corresponding PWDG stability theory; local direction recovery cannot compensate for loss of stability of the continuous or discrete boundary-value problem.

Combining (5.27) with Theorem 5.2 gives the data-to-DG estimate

$$\|u - u_h(\widehat{Z})\|_{\mathrm{DG}} \le C_{\mathrm{qo}} C_{\mathrm{face}}^{1/2} \Big(\sum_K q_K C_{\partial,K}^2 \|c_K\|_2^2 (C_{\log,K} C_{\mathrm{E},K} \|E_K\|_2)^2 \Big)^{1/2}. \tag{5.28}$$

Remark 5.6 (General fields)**.** *If $u = u_{\mathrm{ray}} + r$ and u_{ray} has the form* (5.23)*, the same argument gives*

$$\|u - u_h(\widehat{Z})\|_{\mathrm{DG}} \le C_{\mathrm{qo}} \left(E_{\mathrm{best}} + C_{\mathrm{face}}^{1/2} \Big(\sum_K C_{\partial,K}^2 \|c_K\|_2^2 \delta_K^2 \Big)^{1/2} \right),$$

where E_{best} is the best DG+ *approximation of the nondirectional remainder. The finite-ray case has $E_{\mathrm{best}} = 0$.*

Stability filter and score Approximation is compared only after the recovered candidate is shown to be numerically realizable. For a candidate Z_q define

$$\mathcal{A}_q(Z_q): \quad \max_j |\operatorname{Im} z_j| \le \eta_{\max}, \qquad r_{\mathrm{eff}}(G_q^{\mathrm{PW}}(Z_q); \varepsilon_{\mathrm{solve}}) = q. \tag{5.29}$$

The explicit equispaced spectrum (3.10) remains a cheap capacity estimate for real PW sweeps; the actual selector uses the trace Gram matrix of the recovered real or complex angles.

Algorithm 2 Stability-aware local PW–FB selection

1: compute equilibrated modal data b_m on a resolved window and fix a local budget p;
2: set $\mathcal{Q}(p) = \{p\} \cup \{q : 0 \le q < p,\ p - q = 2M + 1,\ M \in \mathbb{N}_0\}$;
3: **for** $q \in \mathcal{Q}(p)$ **do**
4: if $q > 0$, recover complex angles Z_q by ESPRIT and polish (5.2) subject to $|\operatorname{Im} z_j| \le \eta_{\max}$;
5: reject Z_q unless (5.29) holds;
6: if $q = p$, evaluate the pure-PW trace error; otherwise set $M = (p - q - 1)/2$ and form the full equilibrated PW–FB trace Gram matrix;
7: reject a mixed candidate of effective rank $< p$; otherwise evaluate (3.12);
8: **end for**
9: return the admissible (q, M, Z_q) of minimum trace error.

5.3 Practical resolution and parameter choice

The selector uses only information that is numerically resolved. For a candidate PW rank q, the modal window must be long enough for the shifted ESPRIT system and must remain above the trace-data floor. With the balanced choice above, an odd window of length N permits at most $q \le (N-1)/2$. If no resolved window is long enough for a proposed q, that PW candidate is rejected rather than recovered from coefficients dominated by roundoff. At high frequency the number of significant Fourier modes on a patch grows on the scale of κh; consequently the modal-extraction and Hankel costs also grow. Sparse direction recovery is therefore most advantageous when the number of dominant directions is small compared with this angular bandwidth. For broad angular content, the trace-error comparison naturally favors a larger FB component, as illustrated in Section 6.4.

The rank test and approximation test have different roles. A large $\kappa_H = \sigma_1(H)/\sigma_q(H)$ indicates sensitivity of an assumed rank-q exponential model, but a small κ_H does not imply that the data are close to such a model. Structured nondirectional content can perturb the recovered angles even when the retained signal subspace is well conditioned. Such model mismatch is measured by the residual in (5.2) and ultimately by the trace error in (3.12); a candidate is accepted only after both the numerical-rank test and the approximation comparison. Thus singular values determine whether a rank can be resolved, whereas the trace residual determines whether that rank is an adequate representation.

The containing-disk and physical-boundary routes also use different data. When (3.2) holds, the orthogonal modal coordinates provide the PW–FB comparison developed in Section 3. If it does not hold, the method falls back to weighted Cauchy least squares on ∂K and does not invoke the disk identities or divide by unresolved Bessel factors. This fallback remains a local comparison of candidate spaces; it is not claimed to recover an analytic continuation that does not exist.

5.4 Comparison with globally coupled residual optimization

On a fixed-rank stratum let $z = (z_1, \dots, z_m) \in \mathbb{C}^m$ collect the active complex plane-wave angles. Discrete PW–FB allocations and trace-rank changes are outer events. For fixed z the PWDG state is

$$K(z, \bar{z})c = f(z, \bar{z}), \tag{5.30}$$

and the weighted skeleton residual has the quadratic form

$$\mathcal{J}(c, z, \bar{z}) = c^* R(z, \bar{z})c - c^* b(z, \bar{z}) - b(z, \bar{z})^* c + \gamma(z, \bar{z}), \qquad R = R^* \geq 0. \tag{5.31}$$

This is the matrix form of the jump and boundary residual used in adaptive PWDG (Kapita et al., 2015; Kapita, 2026); R is a residual Gram matrix and is unrelated to the Galerkin matrix K.

Write $z_j = \theta_j + i\eta_j$ and

$$\partial_{z_j} = \tfrac{1}{2}(\partial_{\theta_j} - i\partial_{\eta_j}), \qquad \partial_{\bar{z}_j} = \tfrac{1}{2}(\partial_{\theta_j} + i\partial_{\eta_j}).$$

For the holomorphic local plane wave $\psi_{z_j}(x) = \exp(i\kappa d(z_j) \cdot (x - x_K))$, K_{z_j} differentiates its trial column and $K_{\bar{z}_j}$ the conjugated test row. The coefficient gradient of (5.31) is

$$g_c := \partial_{\bar{c}} \mathcal{J} = Rc - b. \tag{5.32}$$

The DG-constrained residual problem is

$$\Phi_{\mathrm{DG}}(z, \bar{z}) = \mathcal{J}(c(z, \bar{z}), z, \bar{z}), \qquad Kc = f. \tag{5.33}$$

One adjoint solve,

$$K^* \lambda = g_c, \tag{5.34}$$

gives the complete reduced Wirtinger derivative. Indeed, differentiating (5.30) with respect to z_j and $\bar{z}_j$ and eliminating the two coefficient sensitivities yields

$$\begin{aligned} \partial_{\bar{z}_j} \Phi_{\mathrm{DG}} = {} & c^* R_{\bar{z}_j} c - c^* b_{\bar{z}_j} - b_{z_j}^* c + \gamma_{\bar{z}_j} \\ & + (f_{z_j} - K_{z_j} c)^* \lambda + \lambda^* (f_{\bar{z}_j} - K_{\bar{z}_j} c). \end{aligned} \tag{5.35}$$

For the usual conjugated-test load, $f_{z_j} = 0$. Since Φ_{DG} is real, first-order stationarity is simply

$$\partial_{\bar{z}} \Phi_{\mathrm{DG}} = 0. \tag{5.36}$$

If the Galerkin constraint is dropped, fixed-z stationarity is simply $Rc_{\mathrm{LS}} = b$. On a constant-rank stratum,

$$c_{\mathrm{LS}} = R^{\dagger} b, \qquad \Phi_{\mathrm{LS}} = \gamma - b^{*} R^{\dagger} b, \tag{5.37}$$

and the Wirtinger envelope formula is

$$\partial_{\bar{z}_j} \Phi_{\mathrm{LS}} = c_{\mathrm{LS}}^{*} R_{\bar{z}_j} c_{\mathrm{LS}} - c_{\mathrm{LS}}^{*} b_{\bar{z}_j} - b_{z_j}^{*} c_{\mathrm{LS}} + \gamma_{\bar{z}_j}. \tag{5.38}$$

The coefficient derivative disappears because $\partial_{\bar{c}} \mathcal{J} = 0$. This is the complex variable-projection formula (Golub and Pereyra, 1973, 2003). The constrained and unconstrained residual formulations therefore differ only in whether the PWDG state equation is enforced; both are differentiated entirely in Wirtinger coordinates.

The local selector above operates directly at the target frequency and does not require frequency continuation once the modal sequence is resolved. Continuation is used only for the separate globally coupled residual optimization in (5.33).

6 Numerical results

All computations use binary64 arithmetic. Unless stated otherwise, $\tau_{\mathrm{rank}} = 10^{-12}$ and every PWDG solve uses local trace orthonormalization followed by graph–Riesz normalization. Complex-angle optimizations use the bounded strip $|\operatorname{Im} z| \le \eta_{\max}$ with $\eta_{\max} = 1.8$ in the reported experiments.

For the transmission test we reproduce the fluid–fluid interface model of Mascotto and Pichler (2020). The lower and upper half-squares have $\kappa_j = \omega n_j$. For incidence angle θ_i measured from the horizontal interface, set

$$\xi = \kappa_1 \cos\theta_i, \qquad \eta_1 = \kappa_1 \sin\theta_i, \qquad \eta_2 = (\kappa_2^2 - \xi^2)^{1/2}, \quad \operatorname{Re}\eta_2, \operatorname{Im}\eta_2 \ge 0.$$

The exact field is

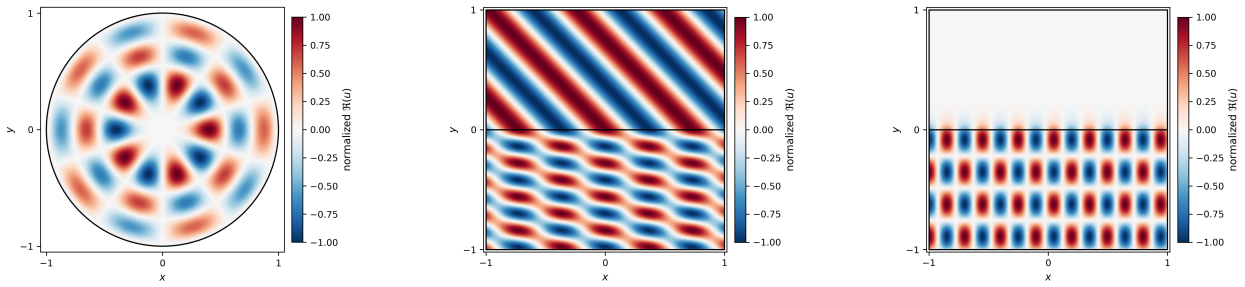
$$u = \begin{cases} e^{i(\xi x + \eta_1 y)} + R e^{i(\xi x - \eta_1 y)}, & y < 0, \\ T e^{i(\xi x + \eta_2 y)}, & y > 0, \end{cases} \qquad R = \frac{\eta_1 - \eta_2}{\eta_1 + \eta_2}, \quad T = \frac{2\eta_1}{\eta_1 + \eta_2}. \tag{6.1}$$

The transmitted complex angle is

$$z_t(\theta_i) = \begin{cases} \arccos(\xi/\kappa_2), & \xi \le \kappa_2, \\ i \operatorname{arcosh}(\xi/\kappa_2), & \xi > \kappa_2. \end{cases} \tag{6.2}$$

For $n_1 = 2$, $n_2 = 1$, $\omega = 12$, the critical angle is $\theta_c = \arccos(\kappa_2/\kappa_1) = 60^{\circ}$. Equation (6.2) is continuous through $z_t = 0$: above 60° it is real, below 60° it is purely imaginary.

Representative exact fields are shown in Fig. 2. The first is the regular Fourier–Bessel solution $J_5(16r)e^{5i\theta}$; the other two are (6.1) on opposite sides of the critical angle. Each panel is a true 2D projection shown with equal x–y scaling, the physical domain boundary, and a visible colormap. Color encodes $\operatorname{Re} u$ after panelwise normalization. The normalization is used only for visualization; all errors below are computed from the unscaled complex fields. In the 29° case the transmitted component loses its oscillatory normal wavenumber and decays exponentially into the upper medium.



(a) Fourier–Bessel solution (b) $\theta_i = 69^\circ$ (c) $\theta_i = 29^\circ$

Figure 2: Representative Helmholtz solutions. (a) A regular Fourier–Bessel solution on the unit disk. (b) Propagating fluid–fluid transmission above the critical angle on $[-1,1]^2$ with interface $y = 0$. (c) Complex-angle transmission below the critical angle; the upper-medium solution decays exponentially away from the interface. The geometry in each panel is shown to scale, and colour represents the panelwise-normalized real part.

6.1 Verification and local selection

We compare the closed formulas of Theorems 3.1, 3.4 and 3.5 with independent boundary quadrature and direct circle least squares. Table 3 gives the largest discrepancy.

Table 3: Verification of the three modal identities against independent direct computation.

identity	comparison	discrepancy
Theorem 3.1	analytical τ_m^2 vs. direct trace quadrature	2×10^{-16}
Theorem 3.4	circulant eigenvalues vs. direct PW Gram spectrum	7×10^{-16}
Theorem 3.5	modal tail least squares vs. direct circle least squares	ratio 1.0000

We next test the selector on exactly representable sparse, broad, and mixed fields. On $B(0, 0.4)$ at $k = 16$, the selector receives only equilibrated modal coefficients and chooses from the same candidate library for three exactly representable fields:

$$u_{\text{ray}} = \sum_{j=1}^{3} c_j e^{ikd(\theta_j)\cdot x}, \quad u_{\text{broad}} = \sum_{m=-4}^{4} b_m J_m(kr) e^{im\theta}, \quad u_{\text{mix}} = u_{\text{ray}} + 0.75\, u_{\text{broad}}, \tag{6.3}$$

with $(\theta_1, \theta_2, \theta_3) = (18^\circ, 71^\circ, 143^\circ)$. The ray count and active harmonics are withheld. Table 4 recovers the generating family and directions.

Table 4: Blind selection for (6.3) at $k = 16$. Active dimension counts retained nonzero local coordinates; the reported error is the relative scaled Cauchy-trace error.

field	q_{PW}	q_{FB}	active dim.	rel. trace error	recovered directions
three rays	3	0	3	6.85×10^{-16}	$18^\circ, 71^\circ, 143^\circ$
broad angular	0	9	9	0	–
mixed	3	9	12	6.71×10^{-16}	$18^\circ, 71^\circ, 143^\circ$

A distributed angular spectrum gives a nontrivial elementwise selection problem on a curved annulus. The reference field is an outgoing Herglotz–DtN solution. Let $d(\phi) = (\cos\phi, \sin\phi)$ and prescribe on $r = a$ the trace of the Herglotz wave $v(x) = \int_0^{2\pi} g(\phi) e^{ikd(\phi)\cdot x} d\phi$ (Colton and Kress, 2001,

2013). With $\widehat{g}_m$ the Fourier coefficients of g, Jacobi–Anger gives $v(a,\theta) = 2\pi \sum_m i^m J_m(ka)\widehat{g}_m e^{im\theta}$. Replacing $J_m(kr)$ by $H_m^{(1)}(kr)$ and matching at $r = a$ gives the outgoing annular field

$$u(r,\theta) = \sum_m c_m H_m^{(1)}(kr) e^{im\theta}, \qquad c_m = \frac{2\pi i^m J_m(ka)\widehat{g}_m}{H_m^{(1)}(ka)}, \tag{6.4}$$

whose Neumann trace on $r = R$ is exactly $\mathrm{DtN}_N u$ with the multiplier of (2.11). The series is truncated at $|m| \le 70$, far beyond the active content at $k = 16$. We use

$$g(\phi) = e^{1.55\cos(\phi-0.48)+0.22\cos(2\phi+0.35)}\, e^{i[0.28\sin(3\phi+0.20)+0.10\cos(5\phi-0.40)]}. \tag{6.5}$$

In contrast to (6.1), the field (6.4) has a genuinely distributed angular spectrum and tests exactly that regime (Fig. 3).

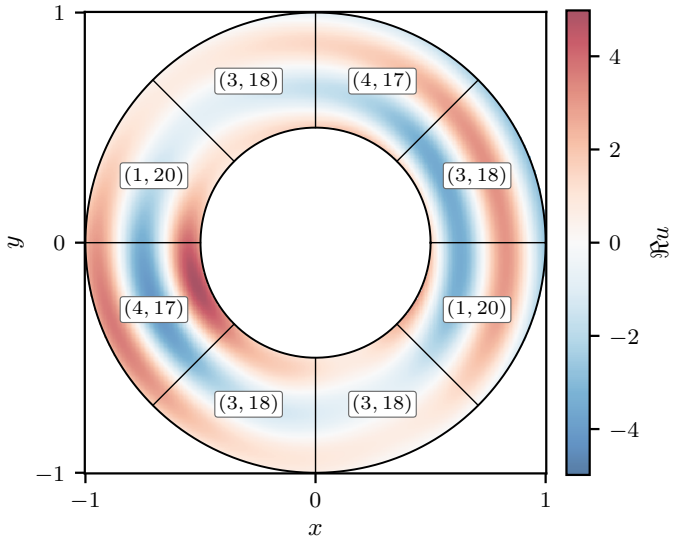


Figure 3: Outgoing Herglotz–DtN reference solution (6.4) with density (6.5) at $k = 16$ on $0.5 \le r \le 1$. The pair $(q_{\mathrm{PW}}, q_{\mathrm{FB}})$ is selected independently on each sector at budget $p = 21$; see Table 5.

For the distributed field (6.4), use eight curved sectors, $|m| \le 70$ in the DtN map, local trace radius $h = 0.44$, and budget $p = 21$. Each element independently chooses $0 \le q_{\mathrm{PW}} \le 4$; the remaining coordinates are centered FB modes. The reference satisfies the truncated DtN relation to relative residual 2.24×10^{-15}.

The selected mesh contains 22 PW and 146 FB coordinates and retains rank 168/168, with $\kappa_{\mathrm{tr,final}} = 1.00000004$ and $\kappa_{\mathrm{GR}} = 2.62$. Its relative global L^2 error is 4.33×10^{-4}, compared with 6.23×10^{-4} for pure FB and 8.83×10^{-4} for equispaced PW at the same nominal dimension.

6.2 High-order stability and estimated traces

On the annulus $0.5 < r < 1$ at $k = 16$, take the exact outgoing field

$$u_{\mathrm{cyl}}(x) = H_0^{(1)}(k|x|). \tag{6.6}$$

Table 5: Elementwise selection for the Herglotz–DtN field at $p = 21$. The last column is the relative best local trace error from (3.12), evaluated before assembly.

element	center angle	q_{PW}	q_{FB}	rel. local trace error
0	22.5°	3	18	9.91×10^{-3}
1	67.5°	4	17	1.29×10^{-2}
2	112.5°	3	18	4.55×10^{-2}
3	157.5°	1	20	3.76×10^{-2}
4	202.5°	4	17	2.89×10^{-2}
5	247.5°	3	18	8.81×10^{-2}
6	292.5°	3	18	3.01×10^{-2}
7	337.5°	1	20	1.58×10^{-2}

The mesh consists of eight exact curved sectors and one radial layer. We impose the exact Dirichlet trace of (6.6) on $r = 0.5$ and the circular DtN condition on $r = 1$, truncated at $|m| \le 70$. Each element starts from p equispaced real plane waves. The local trace disk has center radius 0.75 and radius $h = 0.44$. Before assembly the normalized plane-wave trace Gram matrix is compressed with the fixed numerical-rank threshold $\tau_{\mathrm{rank}} = 10^{-12}$, and the retained trace space is orthonormalized. All quantities in this experiment, including the rank decision, assembly, solve, errors, and condition numbers, are computed in IEEE binary64 arithmetic.

To make the conditioning statements unambiguous, let $G^{\mathrm{tr}}_{K,\mathrm{raw}}$ be the raw local Cauchy-trace Gram matrix and let T_K be the local transformation returned by the trace-rank/compression step. We report

$$\kappa_{\mathrm{tr,raw}} = \max_K \kappa_2(G^{\mathrm{tr}}_{K,\mathrm{raw}}), \qquad \kappa_{\mathrm{tr,final}} = \max_K \kappa_2(T_K^* G^{\mathrm{tr}}_{K,\mathrm{raw}} T_K).$$

With $T = \mathrm{blockdiag}(T_K)$, the assembled matrix in the retained local coordinates is

$$K_h = T^* K_{\mathrm{raw}} T.$$

Thus $\kappa_2(K_h)$ is the condition number *after local trace conditioning but before the global graph–Riesz transformation*. We then form

$$G_h = \frac{K_h^* - K_h}{2i}, \qquad B^* G_h B = I,$$

and the condition number of the matrix actually solved in graph–Riesz coordinates is

$$\kappa_{\mathrm{GR}} = \kappa_2(B^* K_h B). \tag{6.7}$$

These four condition numbers answer different questions: $\kappa_{\mathrm{tr,raw}}$ measures redundancy of the nominal local traces, $\kappa_{\mathrm{tr,final}}$ measures conditioning of the retained local trace coordinates, $\kappa_2(K_h)$ measures the assembled DG operator after the local step, and κ_{GR} measures the final globally transformed linear system.

Table 6: Centered Hankel DtN sweep at $k = 16$. r_K is retained local PW rank and "retained" is the global dimension. The condition columns refer, in order, to the raw local trace Gram, the trace-orthonormalized local Gram, the assembled PWDG matrix, and the final graph–Riesz matrix.

p	nominal	r_K	retained	rel. L^2 error	$\kappa_{\mathrm{tr,raw}}$	$\kappa_{\mathrm{tr,final}}$	$\kappa_2(K_h)$	κ_{GR}
9	72	9	72	5.0086×10^{-1}	2.106×10^{0}	1.0000000	5.646×10^{0}	1.616
15	120	15	120	7.1083×10^{-2}	1.598×10^{0}	1.0000000	3.265×10^{1}	2.106
21	168	21	168	7.2243×10^{-4}	8.627×10^{1}	1.0000000	4.163×10^{2}	2.556
27	216	27	216	1.1688×10^{-5}	5.021×10^{4}	1.0000000	5.728×10^{3}	3.797
33	264	33	264	1.8880×10^{-7}	1.460×10^{8}	1.00000004	6.793×10^{4}	4.941
37	296	37	296	1.6935×10^{-8}	6.072×10^{10}	1.0000158	3.588×10^{5}	6.173
41	328	37	296	1.5608×10^{-8}	4.108×10^{13}	1.0000085	3.493×10^{5}	6.209
49	392	37	296	1.5449×10^{-8}	8.450×10^{16}	1.0000043	3.429×10^{5}	6.189
57	456	37	296	1.5363×10^{-8}	1.681×10^{17}	1.0000039	3.407×10^{5}	6.146
65	520	37	296	1.5517×10^{-8}	4.932×10^{17}	1.0000051	3.438×10^{5}	6.161
73	584	37	296	1.5368×10^{-8}	2.806×10^{17}	1.0000022	3.395×10^{5}	6.148
81	648	37	296	1.5372×10^{-8}	3.189×10^{17}	1.0000045	3.411×10^{5}	6.151
89	712	37	296	1.5326×10^{-8}	3.038×10^{17}	1.0000020	3.388×10^{5}	6.131
97	776	37	296	1.5391×10^{-8}	4.151×10^{17}	1.0000031	3.374×10^{5}	6.125

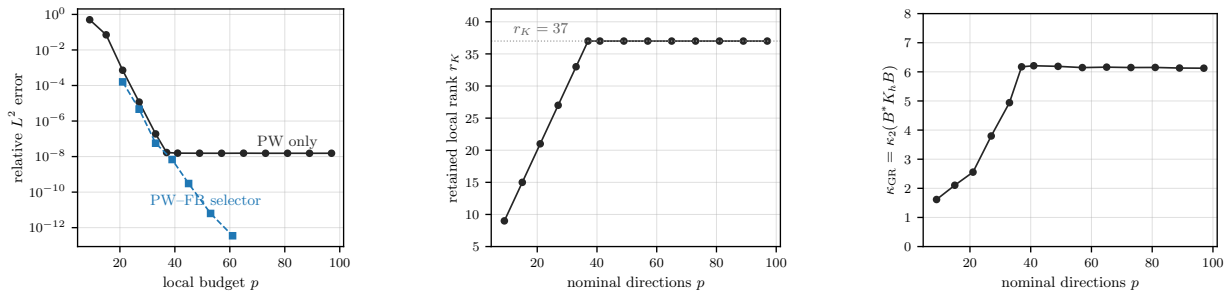


Figure 4: Centered-Hankel DtN experiment. Left: global L^2 error. Centre: retained plane-wave rank. Right: κ_{GR}. The plane-wave-only error stalls when the retained local rank reaches 37, whereas PW–FB selection passes this floor.

The table exposes the practical saturation mechanism directly. Up to $p = 37$ every nominal direction is retained and the global error falls from 5.01×10^{-1} to 1.69×10^{-8}. At $p = 41$ the rank test first rejects unresolved directions: the nominal dimension grows to 328, but the retained dimension stays at 296. From that point through $p = 97$, every element retains exactly 37 directions and the error remains near 1.5×10^{-8}. The high nominal dimensions therefore provide increasingly redundant raw descriptions of essentially the same numerically resolvable local trace space.

The PW-only error floor coincides with local rank saturation at $r_K = 37$: $\kappa_{\mathrm{tr,final}} \approx 1$ and $\kappa_{\mathrm{GR}} \approx 6.1$ even after $\kappa_{\mathrm{tr,raw}}$ enters the binary64 singularity range. The obstruction is therefore local trace resolution, not conditioning of the final solve.

To determine whether Fourier–Bessel coordinates pass the plane-wave ceiling, we repeat the same DtN problem with $q \in \{0, 2, 4, 6\}$ and an FB remainder at fixed budget p. Every candidate is polished in the weighted tail norm and must retain full hybrid trace rank at $\varepsilon_{\mathrm{solve}} = 10^{-12}$.

At $p = 21, 27, 33$ the selector retains two PW directions and an FB block. From $p = 39$ onward

Table 7: PW–FB continuation for the centered Hankel DtN problem. The FB block is $|m| \le M$; retained dimension is measured after local trace orthonormalization.

p	q_{PW}	M	retained	rel. L^2 error	$\kappa_2(K_h)$	κ_{GR}
21	2	9	21	1.5982×10^{-4}	7.232×10^{2}	3.023
27	2	12	27	4.6275×10^{-6}	1.024×10^{4}	3.329
33	2	15	33	5.6434×10^{-8}	1.148×10^{5}	5.732
39	0	19	39	6.8243×10^{-9}	7.132×10^{5}	6.368
45	0	22	45	3.0505×10^{-10}	8.613×10^{6}	7.909
53	0	26	53	6.3124×10^{-12}	2.063×10^{8}	10.685
61	0	30	61	3.5005×10^{-13}	5.416×10^{9}	13.152

the lowest-tail mixed candidates fail the full hybrid rank test, so the selected family becomes pure FB. The error then passes the PW-only rank-37 floor and reaches 3.50×10^{-13} at $p = 61$, while the final matrix has $\kappa_{\mathrm{GR}} = 13.15$.

The rank-threshold sweep in Table 8 shows a stable plateau: 10^{-11} and 10^{-12} retain the same 37 directions and give identical errors, whereas 10^{-13} admits additional directions for which G_h is no longer positive definite in binary64.

Table 8: Rank-threshold sensitivity at $p = 97$. "Fail" means that the assembled G_h is not positive definite in binary64.

τ_{rank}	retained r_K	rel. L^2 error	$\kappa_2(K_h)$	κ_{GR}
10^{-10}	35	4.6080×10^{-8}	1.582×10^{5}	5.864
10^{-11}	37	1.5391×10^{-8}	3.374×10^{5}	6.125
10^{-12}	37	1.5391×10^{-8}	3.374×10^{5}	6.125
10^{-13}	> 37	–	–	Fail

An auxiliary arbitrary-precision local calculation confirms that the nominal PW span continues beyond this binary64 rank ceiling. Tables 6 and 8 concern the realizable binary64 algorithm, including rank selection, assembly, and the final graph–Riesz solve.

The disk radius and rank tolerance are coupled through κh. At $p = 97$ the geometric containing radius of one annular sector is 0.4204; Table 9 varies h just above this value and farther outward. Thus the physical approximation is essentially unchanged when the same 37 trace directions are

Table 9: Trace-radius/rank-threshold sensitivity for the $p = 97$ centered-Hankel test. "Fail" means that the retained floating-point coordinates do not give a positive graph matrix.

h	τ_{rank}	retained r_K	rel. L^2 error	κ_{GR}
0.425	10^{-12}	37	1.538×10^{-8}	6.128
0.440	10^{-12}	37	1.539×10^{-8}	6.125
0.460	10^{-12}	–	Fail	–
0.460	10^{-11}	37	1.540×10^{-8}	6.127
0.500	10^{-11}	–	Fail	–
0.500	10^{-10}	37	1.540×10^{-8}	6.126

retained. Increasing h moves more modal content above a fixed relative threshold, so the threshold must be tightened to the accuracy that the global floating-point solve can actually support. This is the practical reason for choosing a near-minimal admissible disk and for tying τ_{rank} to $\varepsilon_{\mathrm{solve}}$.

We next replace exact selector data by modal data estimated from a coarse numerical field rather than from the exact trace. Starting from nine equispaced PW plus J_0 (relative L^2 error 3.7×10^{-1}),

we estimate modal data, select at budget $p = 21$, solve, and repeat once. Element-boundary Cauchy least squares uses a relative SVD cutoff 10^{-10}. As a comparison, an inscribed-circle estimator at $h_{\mathrm{in}} = 0.24$ inverts factors $J_m(\kappa h_{\mathrm{in}})$ and therefore amplifies high-mode perturbations by $|J_m(\kappa h_{\mathrm{in}})|^{-1}$.

Table 10: Selection from estimated trace data at $p = 21$. Data error is measured in equilibrated modal coordinates; the control uses the exact trace.

stage	estimator	data error	(q_{PW}, M)	rel. L^2 error	κ_{GR}
coarse solve	–	–	–	3.72×10^{-1}	–
cycle 1	element boundary	7.9×10^{-1}	$(2, 9)$	2.24×10^{-4}	2.88
cycle 2	element boundary	1.9×10^{-2}	$(2, 9)$	2.24×10^{-4}	2.88
cycle 1	inscribed circle	7.9×10^{-1}	$(6, 7)$	7.80×10^{-4}	2.63
cycle 2	inscribed circle	4.3×10^{-2}	$(6, 7)$	8.50×10^{-4}	2.55
control	exact trace	0	$(2, 9)$	1.60×10^{-4}	3.02

Boundary-estimated data select the same $(2, 9)$ space as the exact-trace control after one cycle and give error 2.24×10^{-4} versus 1.60×10^{-4} for the control. The inscribed-circle data select $(6, 7)$ and give 7.80×10^{-4}, consistent with the Bessel-factor amplification above.

To test the fallback without a containing disk, consider the L-shaped domain $(-1, 1)^2 \setminus ((0, 1) \times (-1, 0))$ and the corner-singular Helmholtz solution

$$u(r, \theta) = J_{2/3}(\kappa r) \sin(2\theta/3), \qquad 0 \le \theta \le 3\pi/2, \qquad \kappa = 12. \tag{6.8}$$

A representative true solution is shown in Fig. 5. The panel is a true 2D projection on the physical L-shaped domain, displayed to scale with the domain boundary and a visible colormap for the panelwise-normalized real part.

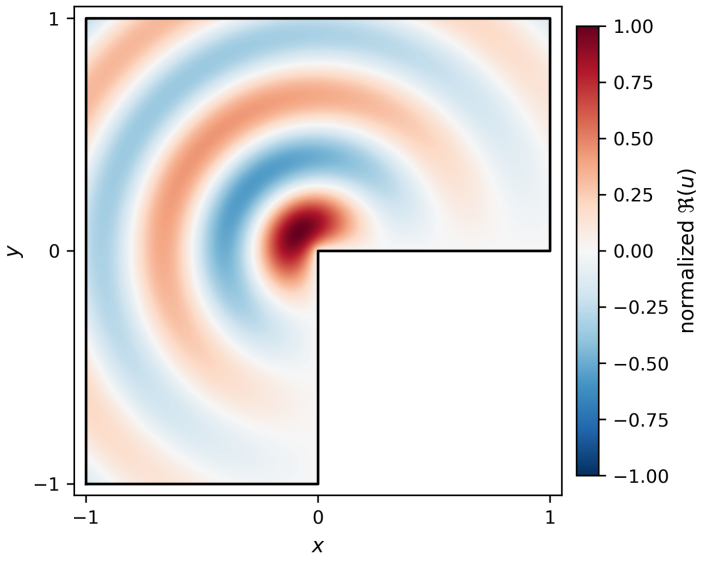


Figure 5: True solution of the L-shaped test problem (6.8) on $(-1, 1)^2 \setminus ((0, 1) \times (-1, 0))$. The geometry is shown to scale, and colour represents the panelwise-normalized real part.

This solution is regular away from the reentrant vertex but is not analytic there. On every triangle the selector therefore fits the exact Cauchy data on ∂K directly. At fixed local budget $p = 7$ it compares $(q_{\mathrm{PW}}, q_{\mathrm{FB}}) = (0, 7)$ and $(2, 5)$; the two PW angles are refined by local variable

Table 11: Boundary-trace selection on the L-shaped corner problem (6.8). The last three columns are global relative L^2 errors at the same local budget $p = 7$.

n	triangles	FB cells	hybrid cells	selector	pure FB	equispaced PW
2	24	4	20	7.35×10^{-1}	1.23	9.52×10^{-1}
3	54	2	52	2.23×10^{-1}	6.01×10^{-1}	6.43×10^{-1}

projection. No global residual search is used. The corresponding graph–Riesz condition numbers are 4.61 and 7.65. This is a coarse robustness test, not a singular-corner convergence theorem: its purpose is to show that the selector remains well defined when (3.2) fails and the comparison is made on the physical element boundary.

6.3 Sparse recovery, complex transmission, and search cost

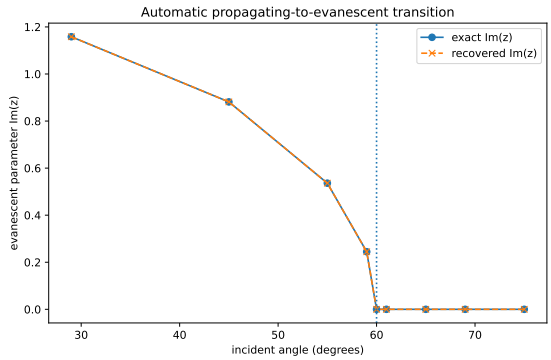
For the three-ray field, ESPRIT recovers the generating directions to about 3×10^{-11} radians. By Theorem 3.6, any PW space containing those directions is exact; Table 12 confirms roundoff-level global error, while equispaced PW and pure FB at the same nominal dimensions remain unresolved.

Table 12: Global relative L^2 error for the three-ray field at $\kappa = 8$. Pure FB uses $(0, p)$; equispaced and direction-identified PW both use $(p, 0)$, so the last two columns isolate the choice of directions.

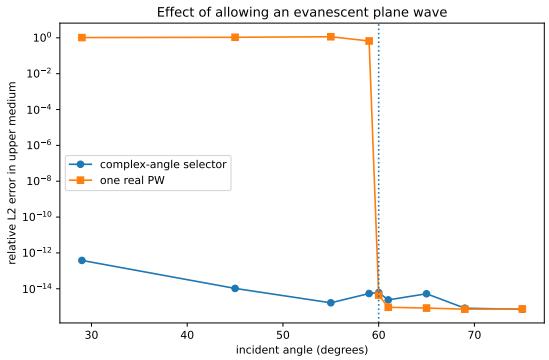
p	FB $(0,p)$	equispaced PW $(p,0)$	identified PW $(p,0)$
5	3.41×10^{-1}	4.73×10^{-1}	5.30×10^{-13}
9	2.87×10^{-2}	4.56×10^{-2}	8.11×10^{-15}
13	9.31×10^{-4}	1.60×10^{-3}	8.94×10^{-14}

Once the three recovered rays are contained in the local space, the exact solution is representable. The variations between 10^{-15} and 10^{-13} in the selector column are therefore floating-point assembly/solve effects and are not expected to decrease monotonically with the nominal budget.

The interface problem now tests the same selector with complex angles. On the eight-triangle mesh take $n_1 = 2$, $n_2 = 1$, $\omega = 12$, $\alpha = \beta = 1/2$, trace radius $h = 0.44$, and two PWs below the interface and one above. Exact Cauchy traces are supplied to isolate the representation problem. The physical angles and the critical angle are not supplied to ESPRIT. For each incidence angle the lower trace recovers the incident and reflected real directions; the upper trace recovers one node ζ_t and hence $z_t = i \operatorname{Log} \zeta_t$.



(a) recovered evanescent parameter



(b) complex versus real transmitted PW

Figure 6: Automatic transition in the fluid–fluid problem (6.1). The dotted line is $\theta_c = 60°$. Left: exact and recovered $\operatorname{Im} z_t$. Right: relative L^2 error in the upper medium using the recovered complex angle and using the same one-PW model constrained to a real angle. No critical-angle test is used by the selector.

The transition is resolved to essentially machine precision. Representative values are given in Table 13. In particular, at 29°,

$$z_t = 1.1582805855\, i,$$

and ESPRIT returns the same imaginary part to 6.4×10^{-14}. The full PWDG error is 5.18×10^{-14} with $\kappa_{\mathrm{GR}} = 2.25$. Constraining the transmitted PW to be real gives upper-medium relative error 1.03; the error is representational, not a failure of the graph-normalized global solve.

Table 13: Automatic propagating-to-evanescent transmission recovery. z_t is the exact complex angle from (6.2); $\widehat{z}_t$ is recovered from the local modal trace. The real-PW column is the upper-medium relative L^2 error when the transmitted PW is constrained to $\operatorname{Im} z = 0$.

θ_i	regime	z_t	$\widehat{z}_t$	global rel. L^2	real-PW upper error	κ_{GR}
69°	prop.	44.214356°	44.214356°	9.77×10^{-16}	7.29×10^{-16}	1.84
60°	grazing	0	$3.6 \times 10^{-17} i$	8.49×10^{-15}	4.43×10^{-15}	1.77
59°	evan.	$0.244649i$	$0.244649i$	4.97×10^{-15}	6.67×10^{-1}	1.77
45°	evan.	$0.881374i$	$0.881374i$	3.20×10^{-14}	1.07	2.45
29°	evan.	$1.158281i$	$1.158281i$	5.18×10^{-14}	1.03	2.25

Finally, we compare local trace selection with the globally coupled residual search on the same approximation family. On the Herglotz–DtN field, both methods optimize the same three shared real PW directions from the same start. The global objective (5.33) assembles and solves PWDG at every trial; the local objective (5.2) performs only elementwise least squares and one final PWDG solve. FB functions are excluded so that the comparison isolates the search objective. The timing comparison likewise isolates this repeated-search cost: any trace sampling or modal projection needed to construct the local data is a one-time preprocessing cost per update and is not included in either nonlinear trial time. Thus Tables 14 and 15 should be read as a comparison of search stages, not as a universal end-to-end speedup when trace acquisition itself is expensive.

The two errors differ by 0.5%, while total search time differs by a factor 27.6. The gain is per trial: 38 ms for the globally coupled objective versus 1.4 ms for the local trace objective.

Repeating the comparison under mesh refinement separates the element-local and globally coupled costs. We repeat the same three-direction Herglotz–DtN search on $(n_\theta, n_r) = (8, 1), (16, 2), (32, 4)$,

Table 14: Cost of global-residual and local-trace selection on the same three-direction Herglotz–DtN problem at $k = 16$. Total time includes the final DG solve.

method	evals	selection (s)	final DG (s)	total (s)	rel. L^2
global residual $\mathcal{J}$	271	10.428	0.145	10.573	7.346×10^{-1}
local Cauchy trace	240	0.346	0.037	0.383	7.383×10^{-1}

using identical starts, tolerances, and nonlinear iteration. Local trials contain only independent element problems; global trials assemble and solve the PWDG system.

Table 15: Search-cost scaling at $k = 16$ on one 2.1 GHz Xeon core. Global trials assemble and solve PWDG; local trials solve only elementwise trace problems.

elements	dofs	per trial (ms)		total (s)		ratio	rel. L^2	
		global	local	global	local		global	local
8	24	6.3	0.31	0.946	0.075	12.6	0.780	0.743
32	96	34.2	1.12	6.810	0.254	26.8	0.564	0.575
128	384	307.8	3.93	58.761	1.240	47.4	0.426	0.460

The local per-trial cost scales approximately with element count, while the total global/local ratio grows from 12.6 to 47.4; the final errors remain within 8% on all three levels.

6.4 Broad and mixed angular content

For a broad 96-direction random-phase Herglotz field, sparse direction identification provides no structural advantage. At moderate dimension, pure FB and equispaced PW have comparable angular reach; at high dimension their difference is stability, because dense PW traces become correlated while equilibrated FB modes remain orthogonal. Table 16 records the FB truncation scale at $p = 17$.

Table 16: Relative Cauchy-trace error of the pure FB truncation at $p = 17$.

spectrum	relative trace error at $p = 17$
sparse directional	8.4×10^{-5}
broad angular	9.3×10^{-5}
mixed	1.0×10^{-4}

At high order, trace equilibration becomes decisive for Fourier–Bessel coordinates. Without FB trace equilibration, the retained global rank stalls at 184 and the error remains near 2.5×10^{-8}. Equilibration retains the full modal dimension and restores high-order convergence (Table 17); this is the scaling effect predicted by Theorems 3.1 and 3.3.

For mixed fields, (3.17) gives the field-dependent exchange points between prescribed candidate spaces. The selector recovers $(3, 9)$ in Table 4, while Table 5 shows spatially varying mixed choices that improve on both pure families at equal nominal dimension.

6.5 ESPRIT capacity and conditioning

This section isolates algebraic direction identification from the DG approximation. Exact modal data are supplied, so the only limits are sample count, Hankel conditioning, and floating-point arithmetic.

Table 17: High-order pure FB spaces $(0, p)$ at $\kappa = 8$ with and without trace equilibration. Parentheses give retained over nominal global graph rank.

p	FB without equilibration	FB with trace equilibration
25	2.45×10^{-8} (184/200)	2.69×10^{-9} (200/200)
33	2.45×10^{-8} (184/264)	1.16×10^{-13} (264/264)

We first fix the modal window and increase the recovered rank. The residual continuation of Kapita (2026) recovered its nested ray family automatically through $q = 19$; its $q = 20$ birth entered a false basin, while a nearby-birth control recovered the same 20-ray space to roundoff. With $N = 81$ exact modal samples, direct ESPRIT instead recovers every admissible rank $q \leq 40$. At the endpoint $q = 40$, the shifted matrix U_0 is square (40×40) and nonsingular; ESPRIT does not require a nullspace of the Hankel matrix. Requesting $q = 41$ violates the shift-dimension condition $q \leq (N - 1)/2$: the shifted signal matrix has only 40 rows and rank 40, and the resulting maximum angular error is 25.30°.

For $N = 401$, the balanced Hankel matrix is 201×201 and Theorem 5.1 permits $q \leq 200$. We retain the first twenty directions and coefficient phases of Kapita (2026); subsequent directions are added deterministically by farthest-point insertion on a 0.05° angular grid, with phases $\phi_j = \mathrm{mod}(0.731j + 0.173j^2, 2\pi) - \pi$ and coefficients $e^{i\phi_j}$.

The error remains near angular roundoff through more than 160 rays and is 8.5×10^{-9} degrees at $q = 184$, where $\kappa_H := \sigma_1(H)/\sigma_q(H) = 6.27 \times 10^4$. At $q = 194$, $\kappa_H = 4.34 \times 10^8$ and the error is 1.08×10^{-4} degrees; at $q = 198$, $\kappa_H = 2.52 \times 10^{12}$ and the error is 1.65°. Thus the high-rank failure is a conditioning limit of the chosen modal window, not a representation limit.

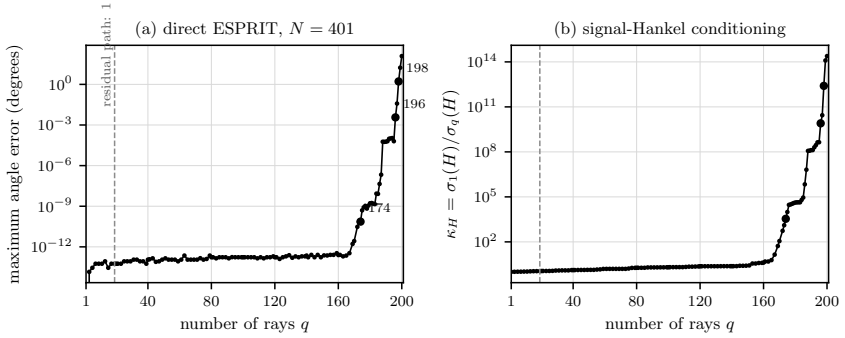


Figure 7: Direct ESPRIT with $N = 401$ target-frequency modal samples. Recovery remains close to roundoff through more than 160 rays; failure near $q = 198$ coincides with growth of $\kappa_H = \sigma_1(H)/\sigma_q(H)$.

The rank limit moves with the modal-window length. For example, $q = 900$ at $N = 2001$ has $\kappa_H = 1.00 \times 10^{12}$ and 1.27×10^{-1} degree error, whereas the same rank at $N = 2201$ has $\kappa_H = 2.16 \times 10^2$ and 9.46×10^{-12} degree error (Table 19). This is consistent with Vandermonde conditioning results for separated nodes (Moitra, 2015; Li and Liao, 2020). The same mechanism governs practical weak or nonideal ray data. With $N = 81$ and three target rays, Table 18 isolates angular separation, amplitude imbalance, and a deterministic 96-direction background. The first two blocks show the expected loss of identifiability through $\sigma_q(H)$. The diffuse case is different: the data are no longer exactly rank three, so κ_H measures conditioning of the retained three-dimensional subspace but not closeness of the data to a three-exponential model. The nonzero angle shift at

Table 18: Finite-ray ESPRIT sensitivity with $N = 81$ modal samples. The background amplitude ρ multiplies a unit-energy 96-direction random-phase field.

perturbation	parameter	max. angle error (deg.)	κ_H
ray separation	1°	2.84×10^{-14}	9.28×10^{1}
ray separation	0.1°	5.15×10^{-13}	9.26×10^{3}
weak-ray amplitude	10^{-4}	2.27×10^{-13}	1.00×10^{4}
weak-ray amplitude	10^{-8}	3.67×10^{-9}	1.00×10^{8}
diffuse background	$\rho = 10^{-2}$	6.21×10^{-3}	2.00
diffuse background	$\rho = 3 \times 10^{-1}$	2.03×10^{-1}	1.94

$\rho = 10^{-2}$ despite $\kappa_H \approx 2$ is therefore model mismatch rather than ill-conditioning, consistent with Theorems 5.2 and 5.6. In the selector this case is not accepted on κ_H alone; the variable-projection residual and the final trace error remain part of the comparison. Practically, a proposed ray is retained only while its signal singular value is above the trace-data floor and the associated reduction of the weighted modal residual is commensurate with the requested accuracy. MUSIC or sparse dictionary methods can be substituted for the initializer, but they do not change the trace metric, hybrid approximation identity, or rank test developed here.

For an $L \times K$ Hankel matrix, a dense SVD costs $O(LK \min\{L, K\})$; a truncated rank-q factorization reduces this to $O(LKq)$ when $q \ll \min\{L, K\}$. The work is element local and parallel. The large windows $N = 401$–2201 below are conditioning stress tests, not default selector sizes; production windows are chosen only large enough to satisfy $L \geq q + 1$, $K \geq q$, and to keep the retained τ_m above the trace-data floor. Since a resolved angular bandwidth typically grows with κh, very high-frequency patches can make a large dense ESPRIT solve unattractive; this is precisely the regime in which a truncated factorization is preferable for sparse content, while broad angular spectra favor FB coordinates.

For the ESPRIT shift fit define

$$\kappa_{\mathrm{sh}} := \kappa_2(U_0) = \frac{\sigma_1(U_0)}{\sigma_q(U_0)}. \tag{6.9}$$

The table shows that κ_{sh} remains modest until the Hankel signal space is already ill-conditioned. This matches Theorem 5.2: the leading amplification is $\sigma_q(H)^{-1}$, followed by the pseudoinverse factor $\sigma_q(U_0)^{-1}$.

Table 19: Representative ESPRIT conditioning data. Increasing the modal window can restore a fixed rank by reducing κ_H.

N	q	max. angle error (deg.)	κ_H	κ_{sh}
1001	400	2.27×10^{-13}	3.66	1.50
1001	470	8.16×10^{-3}	8.04×10^{11}	36.5
1401	580	5.95×10^{-8}	9.17×10^{5}	4.33
2001	900	1.27×10^{-1}	1.00×10^{12}	9.64
2201	900	9.46×10^{-12}	2.16×10^{2}	1.75
2201	940	1.70×10^{-1}	2.93×10^{12}	4.31

7 Conclusions

The central point of this work is that local representation quality and global algebraic conditioning should be treated as separate questions. In the scaled Cauchy-trace geometry, Fourier–Bessel modes

are orthogonal with explicit weights and the same weights generate the spectrum of equispaced plane-wave traces. This identifies two different numerical phenomena: small Fourier–Bessel amplitudes are a scaling effect removable by equilibration, whereas small plane-wave Gram eigenvalues indicate a genuine loss of effective trace dimension. The hybrid identity (3.12) then expresses the best mixed PW–FB approximation as a weighted exponential-fitting problem.

Complex angles require no change in this structure. A propagating or evanescent plane wave generates the same exponential modal sequence, with evanescence encoded by the modulus of its ESPRIT node. The exact-recovery and perturbation results in Theorems 5.1 and 5.2, together with the boundary-trace Lipschitz estimate of Theorem 5.4, yield a direct perturbation-to-PWDG estimate under the standard quasi-optimality hypothesis. After the local space has been fixed, trace-Riesz coordinates and graph–Riesz coordinates act at different levels; Theorem 2.3 shows that the latter produces the normal form $S - iI$.

The computations are consistent with these distinctions. Sparse ray fields are recovered to roundoff, the plane-wave-only high-order experiment stalls when the resolvable local trace rank saturates, and mixed PW–FB spaces pass that floor without degrading the graph-normalized solve. The transmission test crosses from propagation to evanescence without a critical-angle switch in the algorithm. The disk-based modal identities require homogeneous continuation to a containing circle; when this is unavailable, as at the re-entrant corner of the L-shaped test, the same candidate spaces can instead be compared on the physical element boundary.

The practical limits are equally explicit. A PW rank is attempted only when a sufficiently long modal window is resolved above the data and arithmetic floor; 10^{-12} is the binary64 threshold used in the reported calculations, not a universal constant. Strong evanescence enlarges the perturbation constants exponentially through $e^{\kappa h \sinh \eta_{\max}}$, and broad high-frequency angular spectra reduce the advantage of sparse direction recovery. Finally, the perturbation-to-DG estimate inherits the stability assumptions of the underlying PWDG problem and does not regularize a near-resonant boundary-value problem. Extending the analysis to variable coefficients, three-dimensional Trefftz families and fully adaptive meshes requires additional approximation and stability arguments and is left for future work.

Acknowledgements

Generative AI tools were used during manuscript preparation for language editing, typesetting assistance and code assistance. The author verified the mathematical derivations, numerical results and final manuscript content.

Funding

This research received no external funding.

Conflict of interest

The author declares no competing interests.

Data and code availability

Source code for the numerical experiments is available to the editors and referees for the purpose of peer review.

References

Agrawal, A. & Hoppe, R. H. W. (2017) Optimization of plane wave directions in plane wave discontinuous Galerkin methods for the Helmholtz equation. *Port. Math.*, **74**, 69–89.

Amara, M., Chaudhry, S., Diaz, J., Djellouli, R. & Fiedler, S. L. (2014) A local wave tracking strategy for efficiently solving mid- and high-frequency Helmholtz problems. *Comput. Methods Appl. Mech. Engrg.*, **276**, 473–508.

Barnett, A. H. & Betcke, T. (2008) Stability and convergence of the method of fundamental solutions for Helmholtz problems on analytic domains. *J. Comput. Phys.*, **227**, 7003–7026.

Barucq, H., Bendali, A., Diaz, J. & Tordeux, S. (2021) Local strategies for improving the conditioning of the plane-wave ultra-weak variational formulation. *J. Comput. Phys.*, **441**, 110449.

Betcke, T. & Trefethen, L. N. (2005) Reviving the method of particular solutions. *SIAM Rev.*, **47**, 469–491.

Cessenat, O. & Després, B. (1998) Application of an ultra weak variational formulation of elliptic PDEs to the two-dimensional Helmholtz problem. *SIAM J. Numer. Anal.*, **35**, 255–299.

Colton, D. & Kress, R. (2001) On the denseness of Herglotz wave functions and electromagnetic Herglotz pairs in Sobolev spaces. *Math. Methods Appl. Sci.*, **24**, 1289–1303.

Colton, D. & Kress, R. (2013) *Inverse Acoustic and Electromagnetic Scattering Theory*, 3rd edn. Berlin: Springer.

Congreve, S., Gedicke, J. & Perugia, I. (2019) Numerical investigation of the conditioning for plane wave discontinuous Galerkin methods. In *Numerical Mathematics and Advanced Applications, ENUMATH 2017*, Lecture Notes in Computational Science and Engineering, vol. 126, pp. 493–500. Cham: Springer.

Coyle, J. & Nigam, N. (2025) The whys and hows of conditioning of DG plane wave Trefftz methods: a single element. Preprint, arXiv:2509.14500.

Fang, J., Qian, J., Zepeda-Núñez, L. & Zhao, H. (2017) Learning dominant wave directions for plane wave methods for high-frequency Helmholtz equations. *Res. Math. Sci.*, **4**, 9.

Farhat, C., Harari, I. & Franca, L. P. (2001) The discontinuous enrichment method. *Comput. Methods Appl. Mech. Engrg.*, **190**, 6455–6479.

Gittelson, C. J., Hiptmair, R. & Perugia, I. (2009) Plane wave discontinuous Galerkin methods: analysis of the h-version. *ESAIM Math. Model. Numer. Anal.*, **43**, 297–331.

Golub, G. H. & Pereyra, V. (1973) The differentiation of pseudo-inverses and nonlinear least squares problems whose variables separate. *SIAM J. Numer. Anal.*, **10**, 413–432.

Golub, G. & Pereyra, V. (2003) Separable nonlinear least squares: the variable projection method and its applications. *Inverse Problems*, **19**, R1–R26.

Golub, G. H. & Van Loan, C. F. (2013) *Matrix Computations*, 4th edn. Baltimore: Johns Hopkins University Press.

Hiptmair, R., Moiola, A. & Perugia, I. (2011) Plane wave discontinuous Galerkin methods for the 2D Helmholtz equation: analysis of the p-version. *SIAM J. Numer. Anal.*, **49**, 264–284.

Hiptmair, R., Moiola, A. & Perugia, I. (2016a) Plane wave discontinuous Galerkin methods: exponential convergence of the hp-version. *Found. Comput. Math.*, **16**, 637–675.

Hiptmair, R., Moiola, A. & Perugia, I. (2016b) A survey of Trefftz methods for the Helmholtz equation. In *Building Bridges: Connections and Challenges in Modern Approaches to Numerical Partial Differential Equations*, Lecture Notes in Computational Science and Engineering, vol. 114, pp. 237–279. Cham: Springer.

Hua, Y. & Sarkar, T. K. (1990) Matrix pencil method for estimating parameters of exponentially damped/undamped sinusoids in noise. *IEEE Trans. Acoust. Speech Signal Process.*, **38**, 814–824.

Huttunen, T., Monk, P. & Kaipio, J. P. (2002) Computational aspects of the ultra-weak variational formulation. *J. Comput. Phys.*, **182**, 27–46.

Kapita, S. (2026) Direction-adaptive plane-wave discontinuous Galerkin methods for the Helmholtz equation. Preprint, arXiv:2608.18380.

Kapita, S. & Monk, P. (2018) A plane wave discontinuous Galerkin method with a Dirichlet-to-Neumann boundary condition for the scattering problem in acoustics. *J. Comput. Appl. Math.*, **327**, 208–225.

Kapita, S., Monk, P. & Warburton, T. (2015) Residual-based adaptivity and PWDG methods for the Helmholtz equation. *SIAM J. Sci. Comput.*, **37**, A1525–A1553.

Keller, J. B. & Givoli, D. (1989) Exact non-reflecting boundary conditions. *J. Comput. Phys.*, **82**, 172–192.

Kreutz-Delgado, K. (2009) The complex gradient operator and the CR-calculus. Preprint, arXiv:0906.4835.

Li, W. & Liao, W. (2020) Stable super-resolution limit and smallest singular value of restricted Fourier matrices. *Appl. Comput. Harmon. Anal.*, **51**, 118–156.

Li, W., Liao, W. & Fannjiang, A. (2020) Super-resolution limit of the ESPRIT algorithm. *IEEE Trans. Inform. Theory*, **66**, 4593–4608.

Luostari, T., Huttunen, T. & Monk, P. (2012) The ultra weak variational formulation using Bessel basis functions. *Commun. Comput. Phys.*, **11**, 400–414.

Mallat, S. G. & Zhang, Z. (1993) Matching pursuits with time-frequency dictionaries. *IEEE Trans. Signal Process.*, **41**, 3397–3415.

Mascotto, L. & Pichler, A. (2020) Extension of the nonconforming Trefftz virtual element method to the Helmholtz problem with piecewise constant wave number. *Appl. Numer. Math.*, **155**, 160–180.

Moiola, A., Hiptmair, R. & Perugia, I. (2011) Plane wave approximation of homogeneous Helmholtz solutions. *Z. Angew. Math. Phys.*, **62**, 809–837.

Moitra, A. (2015) Super-resolution, extremal functions and the condition number of Vandermonde matrices. In *Proceedings of the 47th Annual ACM Symposium on Theory of Computing (STOC 2015)*, pp. 821–830. New York: ACM.

Monk, P. & Wang, D.-Q. (1999) A least-squares method for the Helmholtz equation. *Comput. Methods Appl. Mech. Engrg.*, **175**, 121–136.

Nelder, J. A. & Mead, R. (1965) A simplex method for function minimization. *Comput. J.*, **7**, 308–313.

Parolin, E., Huybrechs, D. & Moiola, A. (2023) Stable approximation of Helmholtz solutions in the disk by evanescent plane waves. *ESAIM Math. Model. Numer. Anal.*, **57**, 3499–3536.

Perrey-Debain, E. (2006) Plane wave decomposition in the unit disc: convergence estimates and computational aspects. *J. Comput. Appl. Math.*, **193**, 140–156.

Potts, D. & Tasche, M. (2013) Parameter estimation for nonincreasing exponential sums by Prony-like methods. *Linear Algebra Appl.*, **439**, 1024–1039.

Roy, R. & Kailath, T. (1989) ESPRIT: estimation of signal parameters via rotational invariance techniques. *IEEE Trans. Acoust. Speech Signal Process.*, **37**, 984–995.

Stewart, G. W. & Sun, J.-G. (1990) *Matrix Perturbation Theory*. Boston: Academic Press.

Watson, G. N. (1944) *A Treatise on the Theory of Bessel Functions*, 2nd edn. Cambridge: Cambridge University Press.

Wax, M. & Kailath, T. (1985) Detection of signals by information theoretic criteria. *IEEE Trans. Acoust. Speech Signal Process.*, **33**, 387–392.

Wedin, P.-Å. (1972) Perturbation bounds in connection with singular value decomposition. *BIT*, **12**, 99–111.